American Journal of Botany 91(3): 369–385. 2004.

ANALYSIS OF CIRCULAR BORDERED PIT FUNCTION I. ANGIOSPERM VESSELS WITH HOMOGENOUS PIT MEMBRANES[1]

JOHN S. SPERRY[2] AND UWE G. HACKE

Biology Department, University of Utah, 257 South 1400 East, Salt Lake City, Utah 84112 USA

A model predicted pit and vessel conductivity, the air-seed pressure for cavitation, and the implosion pressure causing vessel collapse. Predictions were based on measurements from 27 angiosperm species with circular bordered pits and air-seed pressures of 0.2–11.3 MPa. Vessel implosion pressure exceeded air-seed pressure by a safety factor of 1.8 achieved by the increase in vessel wall thickness per vessel diameter with air-seed pressure. Intervessel pitting reduced the implosion pressure by 20 to 40%. Pit hydraulic conductivity decreased by 30-fold from low (<1 MPa) to high (>10 MPa) air-seed pressure primarily because of decreasing pit membrane conductivity. Vessel conductivity (per length and wall area) increased with vessel length as higher lumen conductivity overcame low pit conductivity. At the "saturating vessel length," vessel conductivity maximized at the Hagen-Poiseuille value for the lumen per wall area. Saturated vessel conductivity declined by sixfold with increasing air-seed pressure because of increased wall thickness associated with increased implosion resistance. The saturated vessel length is likely the optimal length because: (a) shorter vessels have lower conductivities, (b) longer vessels do not increase conductivity when functional yet decrease it more when cavitated, (c) observed pit structure most closely optimized vessel conductivity at the saturated length, and (d) saturated lengths were similar to measured lengths.

Key words: functional wood anatomy; hydraulic architecture; plant biomechanics; plant water transport; xylem cavitation; xylem hydraulic conductivity.

Xylem conduit walls must perform three important functions: (1) permit water flow between adjacent conduits, (2) prevent air entry from embolized (gas-filled) conduits to adjacent water-filled functional ones, and (3) prevent implosion under the significant negative pressure of the transpiration stream (Zimmermann, 1983; Carlquist, 1988). These functions are fulfilled by a thick lignified wall for strength that is punctuated with thin areas (pits) to allow water flow (Fig. 1). The pits lack thick secondary wall layers, and the thin compound middle lamella of adjacent primary cell walls is modified to form a relatively porous pit membrane. The surrounding secondary wall arches over the pit membrane, forming a pit border with an aperture opening to the inner pit chamber (Fig. 1C, D). The first function is in direct conflict with the other two because the wall features that prevent air entry (strong pit membranes with narrow pores) and implosion (thick, lignified wall layers with few pits) also inhibit water flow.

Presumably, the structure of the xylem conduits optimizes these conflicting functions to some degree, providing the necessary hydraulic conductivity with the least investment in wall material and at a given safety from air-seeding and implosion. The structure of the interconduit pit itself has long been assumed to reflect a beneficial compromise between maintaining wall strength and safety from embolism on the one hand vs. promoting water flow on the other (Carlquist, 1988). The arching border of circular bordered pits places compressively strong lignified wall material far from the neutral axis where it can withstand the bending forces best. The aperture, though relatively narrow, has a conductivity much greater than an equal area of pit membrane. The open pit chamber exposes maximal surface area of this limiting membrane without weakening the wall. The membrane is relatively thin, nonlignified and hence, porous and hydrophilic. This enhances hydraulic conductivity when water is on both sides, but also minimizes the air-seeding of cavitation through the pit when an air-water interface becomes drawn into the pit membrane.

Intuitively, a pit that is more resistant to air-seeding should also be less conductive to water. If so, this could be one reason for the observed correlation between a species' air-seed pressure and the severity of water stress it must endure (Davis et al., 1999; Hacke et al., 2000; Pockman and Sperry, 2000). The xylem should be no more resistant to air-seeding than it has to be if in doing so it unnecessarily sacrifices hydraulic conductivity. The variation in pit shape and membrane structure may be adaptive in optimally balancing the conflict between conductivity and safety from air-seeding.

Perhaps the most striking difference between pit types is the contrast between the typical "homogenous" pit membrane of wide phylogenetic distribution that is uniformly thin and microporous vs. the torus-margo structure of many gymnosperm tracheids. The two membrane types represent different solutions to the same problem; but it seems likely that they may have quite different hydraulic conductivities for the same air-seed pressure (Lancashire and Ennos, 2002).

In addition to being influenced by pit structure, the hydraulic conductivity of a conduit is also determined by the width and length of the conduit lumen. According to the Hagen-Poiseuille equation, hydraulic conductivity of the lumen should increase with the fourth power of the conduit width. This gain in conductivity can only be realized, however, if the lumen is sufficiently long so that the pit conductivity is not limiting. The work of Gibson and colleagues (Calkin et al., 1986; Schulte et al., 1987; Schulte and Gibson, 1988) has shown that tracheid length must increase with tracheid diam-

[1] Manuscript received 1 July 2003; revision accepted 21 October 2003.

The authors wish to thank Professor Larry DeVries of the University of Utah Mechanical Engineering Department and Professor Fred Adler of the University of Utah Biology Department for numerous discussions concerning the modeling of stresses and strains in the xylem. This research was supported by NSF grant IBN-0112213.

[2] E-mail: sperry@biology.utah.edu.

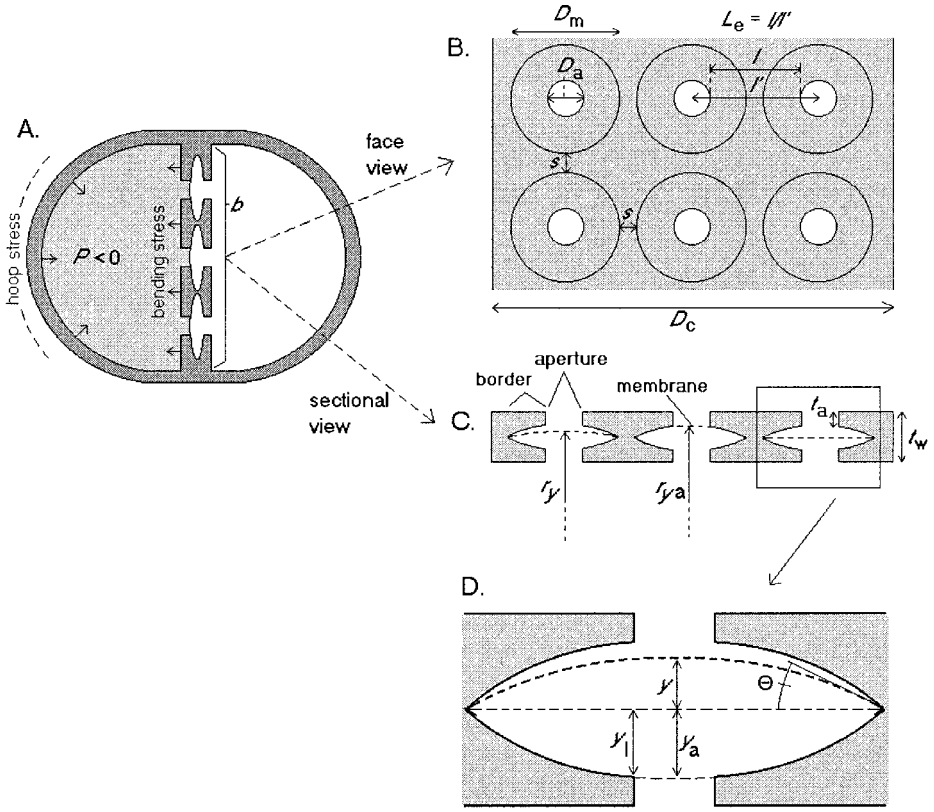

Fig. 1. Relevant features of angiosperm vessel wall structure. (A) Transverse view of two adjacent conduits and pitted wall. Negative pressure in water-filled conduits induces circumferential hoop stresses in the conduit wall. Larger bending stresses are induced when the adjacent conduit is air-filled and the common wall bends towards the water-filled side. b = width of the pitted common wall. (B) Face view of pitted wall. D_a = aperture diameter; D_m = membrane diameter; s = spacing between pits; L_e = ligament efficiency (ratio of dimensions l/l'). (C) Transverse view of pitted wall showing pit aperture, border, and membrane. r_y = radius of curvature of membrane deflected distance y from flat position; r_{ya} = radius of curvature of inner chamber wall; t_w = double wall thickness; t_a = thickness of single aperture. (D) Median transverse section through a single pit: y = membrane deflection from flat position; y_a = membrane deflection for radius of curvature = r_{ya}; y_l = distance from flat membrane to inner edge of aperture; Θ = angle of membrane deflection from flat position.

eter if there is to be a net gain in total tracheid conductivity, and this is presumably why tracheid diameter and length are correlated. The same principle applies for vessels where length and diameter are also positively related (Ewers and Fisher, 1989).

Adjustments in conduit diameter and length may compensate for the changes in pit conductivity associated with different air-seed pressures. Thus, a species capable of avoiding cavitation by air-seeding and necessarily having low-conductivity pits does not necessarily have to have a low overall conductivity if the conduit width and length increase to overcome the added pit resistance. The interaction between pit and lumen conductivity may underlie the variable relationship between cavitation resistance and xylem conductivity, with some researchers showing a trade-off of varying significance and others showing no relationship at all (Sperry and Saliendra, 1994; Tyree et al., 1994; Davis et al., 1998; Pockman and Sperry, 2000; Hacke and Sperry, 2001; Martinez-Vilalta et al., 2002).

In this series of two papers, we present a model that predicts the three functions of pitted conduits—hydraulic conductivity, air-entry pressure (= "air-seed pressure"), and mechanical strength—from conduit structure. For simplicity, we confine ourselves to species with circular bordered pits. The model extends Petty's mechanical analysis of pit membranes (Petty, 1972), our previous study of conduit wall strength against implosion (Hacke et al., 2001a), and several previous studies of tracheid conductivity (Calkin et al., 1986; Schulte and Gibson, 1988; Lancashire and Ennos, 2002) to account for all three conduit functions with a relatively simple set of calculations.

In this first paper, we describe the model in detail and apply it to the uniformly thin and homogenous pit membrane structure typical of intervessel pits of angiosperms. We compare the model to data from root and stem xylem of 27 angiosperm species with measured air-seed pressures ranging from 0.2 to 11.3 MPa, hence, reflecting the broad range of negative pressure exhibited by vascular plants (Table 1). We evaluated the trade-offs between the three functions and considered the extent to which vessel structure has optimized conductivity per investment in conduit structure and per air-seed pressure.

In the second paper of the series (Hacke et al., 2004), we describe extensions of the model to the torus-margo pit structure of gymnosperm tracheids and evaluate tracheid structure and function in comparison with the results for vessels.

MATERIALS AND METHODS

The data set and air-seed pressure (P_a)—The data set was largely compiled from previous studies, including a comparative analysis of cavitation resistance and wood density (Hacke et al., 2001a). The most important criterion was to have a wide range of cavitation resistance for comparison with conduit

TABLE 1. Study species listed alphabetically by family. Habitats are Wasatch Mountains of Utah (WM), Piedmont of North Carolina (NC), Utah's Great Basin (GB), greenhouse-grown plants (GH), Sonoran Desert (SD), California Chaparral (CC), Pepperdine University campus (PP). In some species, both stem (S) and root (R) organs were measured. In rice, leaves (L) were measured. The air-seed pressure (P_a) is the absolute value of the negative pressure required to eliminate 50% of the hydraulic conductivity of the xylem sample. When two P_a values are given, the second one refers to roots. Data source is given where measurements were not made specifically for this paper.

Species	Family	Organ	Habitat	P_a (MPa)	Source
Acer grandidentatum	Aceraceae	S, R	WM	4.0, 0.8	
A. negundo	Aceraceae	S, R	WM	2.4, 0.3	Hacke et al., 2001b
A. rubrum	Aceraceae	S	NC	3.3	
Nerium oleander	Apocynaceae	S	PP	1.7	
Baccharis salicifolia	Asteraceae	S	SD	3.0	Pockman and Sperry, 2000
Chrysothamnus nauseosus	Asteraceae	R	GB	2.1	Sperry and Hacke, 2002
C. parryi	Asteraceae	R	GB	2.7	Sperry and Hacke, 2002
C. viscidiflorus	Asteraceae	R	GB	1.7	Sperry and Hacke, 2002
Helianthus annuus	Asteraceae				
(well-watered)		S	GH	1.7	Stiller and Sperry, 2002
(drought-grown)		S	GH	3.5	Stiller and Sperry, 2002
Tetradymia glabrata	Asteraceae				
(fine soil habitat)		R	GB	3.2	Sperry and Hacke, 2002
(coarse soil habitat)		R	GB	1.8	
Alnus incana	Betulaceae	S, R	WM	1.6, 0.2	Hacke et al., 2001b
Betula occidentalis	Betulaceae	S, R	WM	1.3, 0.3	Hacke et al., 2001b
Acacia constricta	Fabaceae	S	SD	6.0	Pockman and Sperry, 2000
A. greggii	Fabaceae	S	SD	5.4	Pockman and Sperry, 2000
Prosopis velutina	Fabaceae	S	SD	6.2	Pockman and Sperry, 2000
Laurus nobilis	Lauraceae	S	GH	1.7	Hacke and Sperry, 2003
Fraxinus velutina	Oleaceae	S	SD	2.7	Pockman and Sperry, 2000
Oryza sativa	Poaceae				
(IR 64)		L	GH	1.9	Stiller et al., 2003
(Azucena)		L	GH	1.9	Stiller et al., 2003
Ceanothus crassifolius	Rhamnaceae	S	CC	9.4	Davis et al., 2002
C. cuneatus	Rhamnaceae	S	CC	9.5	Davis et al., 1999
C. oliganthus	Rhamnaceae	S	CC	6.2	Davis et al., 1999
C. megacarpus	Rhamnaceae	S	CC	11.0	Davis et al., 1999
Adenostoma fasciculatum	Rosaceae	S	CC	8.3	Davis et al., 1998
Prunus virginiana	Rosaceae	S	WM	3.8	
Populus fremontii	Salicaceae	S	SD	2.1	Pockman and Sperry, 2000
Populus angustifolia	Salicaceae	S	WM	1.9	Hacke et al., 2001b
Larrea tridentata	Zygophyllaceae	S	SD	11.3	Pockman and Sperry, 2000

structure. The cavitation resistance of each xylem sample in the data set is represented by the "air-seed pressure (P_a)" (Table 1), which is the pressure difference (a positive value) required to force air into the xylem conduits and cause cavitation. It is equal and opposite to the negative sap pressure at cavitation. It was obtained from vulnerability curves measured with the centrifugal force method (Pockman et al., 1995) on $n \geq 6$ xylem samples per species and organ (usually stems or roots). Segments 14 cm long were flushed at 100 kPa with deionized, filtered (0.2 μm) water to remove any xylem embolism. The maximum hydraulic conductivity of each segment was subsequently measured with a conductivity apparatus (Sperry et al., 1988). Then, segments were spun in a centrifuge to a known xylem pressure (Pockman et al., 1995). After spinning, the loss of hydraulic conductivity was measured and plotted vs. the corresponding xylem pressure to obtain vulnerability curves. Shoots were 5–13 mm in diameter. Root diameter ranged from 3 to 13 mm. The air-seed pressure of a xylem sample was represented by the pressure required to cause a 50% loss of hydraulic conductivity by cavitation (the absolute value of P_{50} sensu Hacke et al., 2001a). By including species from numerous diverse habitats, we were able to obtain a wide range of P_a from a minimum of 0.2 MPa in *Alnus incana* roots to a maximum of 11.3 MPa in *Larrea tridentata* stems (Table 1).

It was important to sample broadly across phylogenetic lineages, growth form, and organ to include these potential sources of variation in structure that might be independent of variation in cavitation resistance. The 27 species are in 12 families of widespread phylogenetic affinity, including herbs, woody shrubs, and trees (Table 1). Stem and root measurements were available, as well as leaf data from one species (*Oryza sativa*). Roots tend to be more vulnerable to cavitation than stems (Sperry and Saliendra, 1994; Mencuccini and Comstock, 1997; Kolb and Sperry, 1999a; Hacke et al., 2000). This was also seen in the present data set where root P_a averaged 1.9 MPa less than stem P_a for the four species with data for both organs.

Anatomical measurements—Pit and conduit dimensions (Fig. 1) were measured on the same or similar xylem samples used to determine the P_a. Measured parameters included the hydraulic mean conduit diameter: $D_c = \Sigma d_c^5 / \Sigma d_c^4$, where d_c = individual conduit diameter (Kolb and Sperry, 1999b). The D_c represents the size of a conduit cavitating at P_a under the following conditions. (1) A normal distribution of hydraulic conductivity vs. d_c for a xylem sample. This means that 50% of the hydraulic conductivity will occur in conduits greater than D_c and 50% will occur in conduits narrower than D_c. (2) Wider conduits have lower air-seed pressures than narrower ones within a xylem sample. Thus, the pressure causing a 50% loss of hydraulic conductivity (the P_a) will be the cavitation pressure of a vessel of diameter D_c. Both conditions are consistent with observations (Salleo and Lo Gullo, 1989; Lo Gullo and Salleo, 1993; Hargrave et al., 1994).

Conduit dimensions were measured in transverse freehand sections stained with phloroglucinol-HCl. To determine the D_c, lumen area was measured for all vessels in radial sectors of recent growth rings from each xylem sample used to determine the P_a. The d_c was calculated as the diameter of a circle with the same lumen area, and D_c was calculated for each xylem sample before the mean D_c was obtained for all samples. The thickness of intervessel walls (t_w; Fig. 1C) was measured only for conduit pairs that averaged within ±3 μm of D_c. The width of the common wall (*b*, Fig. 1A) was assumed equal

to D_c. This proved to be a better approximation for vessels than using the side of a square of equal area to the conduit lumen as used previously (Hacke et al., 2001a).

Pit dimensions were measured in longitudinal freehand sections stained with phloroglucinol-HCl. All species had circular bordered pits. Photographs were taken with a digital camera attached to a light microscope under oil immersion at 1000× magnification. The diameter of the pit membrane (D_m) and pit aperture (D_a; Fig. 1B) was measured with standard image analysis software on $n \geq 10$ pits per plant organ and species. For irregular pit aperture shapes, the aperture diameter was calculated as the diameter of a circle with an area equal to the aperture area. Definitions of symbols are provided in Table 2.

MODEL DESCRIPTION

The model was designed to provide three predictions from conduit structure: (1) the strength of the conduit walls against implosion, (2) the air-seed pressure, (3) the conductivity of the vessel, including both lumen and pit components, expressed per transverse sectional wall area. Table 2 summarizes the model parameters by listing: (a) constants, (b) input variables either taken from direct measurements or input in incremental fashion for observing the effect on output variables, (c) output variables.

Conduit implosion pressure (P_i)—The negative water pressure in functional conduits pulls inward on the conduit wall, creating mechanical stress. If this stress exceeds the wall strength, the wall will buckle inwards, or implode. The largest wall stress occurs when a water-filled conduit abuts an air-filled one, causing the common wall to bend towards the water-filled side (Fig. 1A). These bending stresses are greater than the circumferential hoop stresses girdling the entire wall (Hacke et al., 2001a) and are the focus of the implosion analysis. The implosion pressure (P_i) was defined as the pressure difference between water and air on either side of the wall (a positive number) that was necessary to cause the bending stress to exceed the wall strength. While the implosion pressure can exceed the air-seed pressure, the reverse seems unlikely in lignified conduits because as the wall implodes it should trigger air-seeding and cavitation—thus eliminating the pressure difference. If so, conduit walls should exhibit a P_i/P_a ratio (the implosion safety factor) of one or more.

The implosion pressure was estimated from conduit dimensions using standard mechanical engineering equations (Young, 1989). These equations assume that the solid cell wall material has the same mechanical properties in all directions (isotropic) and that the wall structure conforms to relatively simple geometries for which there are analytical approximations for maximum stresses and strains. Neither condition is completely true but it is appropriate to start with a simple approach.

We build on an earlier analysis of implosion pressure (P_i) that ignored pits and estimated wall stress, assuming the wall is a flat solid plate of finite width b and effectively infinite length (Young, 1989; Hacke et al., 2001a):

$$P_i = (W/\beta)(t_w/b)^2 \quad (1)$$

where W is wall strength, β is a coefficient that depends on the width-to-length ratio of the wall (=0.25 for a ratio of 0.5 or less), and t_w is the thickness of the double wall. Here we add the weakening effect of pits based on the analysis by O'Donnell and Langer (1962) on the bending stresses of perforated plates. Regularly spaced perforations increase the stress in a solid plate in inverse proportion to their "ligament efficiency" (L_e). The ligament efficiency is the minimum distance between the edges of the holes divided by the distance between the hole centers (Fig. 1B). In terms of the circular bordered pit,

$$L_e = 1 - [D_a/(D_m + s)] \quad (2)$$

where s is the minimum horizontal distance between pit edges (Fig. 1B). P_i becomes

$$P_i = (W/\beta)(t_w/b)^2 L_e. \quad (3)$$

Equation 3 neglects the presence of a pit chamber. The bulk of the chamber volume is located near the neutral plane of bending (the pit membrane), and it should not weaken the wall much compared to a solid wall. Nevertheless, to account for its effect, we calculated the ratio of the second moment of area (I) for a median section through a circular bordered pit with (I_h) and without (I_s) a chamber present. Equation 3 assumes that $P_i \propto WI_s$, so multiplying the right-hand side by the (I_h/I_s) ratio corrects for the presence of a chamber. The irregular geometry of the pit section required a numerical calculation of I. The I_h/I_s ratio was calculated for the median section where it would be smallest and represents a liberal estimate of the weakening effect of a chamber. The complete calculation of P_i was:

$$P_i = (W/\beta)(t_w/b)^2 L_e(I_h/I_s). \quad (4)$$

We used Eq. 4 to calculate the P_i from measured values of L_e, the "thickness-to-span ratio" $(t_w/b)^2$, and estimates of the minimum "moment ratio" (I_h/I_s).

Air-seed pressure (P_a)—Two modes of air-seeding were considered (Fig. 2). "Capillary-seeding" occurs by the failure of the air–water meniscus in a preexisting pit membrane pore (Fig. 2A). It occurs at a pressure difference, P_c, sufficient to overcome the capillary force of the meniscus (Pickard, 1981; Zimmermann, 1983).

"Rupture-seeding" occurs through pores created by membrane rupture—structural failure of the membrane that creates holes large enough for air-seeding to occur (Fig. 2B). Rupture-seeding occurs at a pressure difference across the membrane, P_r, that causes the stress in the membrane to exceed its strength. The air-seed pressure, P_a, of a given membrane will be determined by which pressure—P_c or P_r—is reached first as the membrane is deflected by the air-water interface (e.g., Fig. 3).

To calculate the air-seed pressure, we extended Petty's (1972) analysis of how the pressure difference across the membrane relates to its displacement (strain) and the stress in its load-bearing elements. The analysis assumed a linear stress–strain relationship for the load-bearing microfibrils of the pit membrane and circular-bordered-pit geometry. When an air–water interface is pulled into the membrane, capillarity exerts an acting force normal to the membrane equal to the pressure difference (P) multiplied by the membrane area:

$$\text{acting force} = P\pi D_m^2/4. \quad (5)$$

At equilibrium, this acting force is balanced by a re-acting tensile force in the membrane. Petty assumed that the most important load-bearing elements in the membrane are the radial "spokes" of microfibrils running across the membrane center (Fig. 4). The total resisting force is then the sum of the

TABLE 2. List of parameters in the pit model with symbol, dimension (l, length; f, force; p, pressure [f · l^{-2}]; t, time), definition, and for constants, the values employed.

Symbol	Dimension	Definition
Constants		
A_f	l^2	cross-sectional area of microfibril spokes = 707 nm^2
a	degree	contact angle of air-water meniscus = 0°
E	f · l^{-2}	modulus of elasticity of microfibril spokes; default = 5 GPa
e_{ya}	—	spoke strain at aspiration = 0.03
F	f · l^{-2}	strength of microfibril spokes; default = 2.2 GPa
s_f	l	spacing between parallel microfibrils in a sheet; default = 1.5 μm
t_t	l	thickness of microfibril strand = 30 nm
W	f · l^{-2}	strength of solid wall at saturation = 80 MPa
X	—	pitting coefficient; default = 2
υ	pt	viscosity of water at 20°C = 0.001 Pa s
τ	f · l^{-2}	surface tension of water at 20°C = 0.0728 N · m^{-1}
Input variables		
b	l	width of pitted wall between vessels
D_c	l	hydraulic mean conduit diameter
D_a	l	pit aperture diameter
D_m	l	pit membrane diameter
L	l	conduit length
P_a	p	air-seed pressure = $-P_{50}$ sensu Hacke et al. (2001a)
t_w	l	thickness of double conduit wall
Output variables		
A_w	l^2	cross-sectional wall area of vessel
D_p	l	maximum pore diameter in relaxed membrane
D_p'	l	maximum pore diameter in stretched membrane
D_{pe}	l	equivalent pore diameter for membrane conductivity
e, e_y	—	spoke strain (e) at membrane displacement y (e_y)
h	—	fraction of membrane area occupied by pores
I_s	l^4	second moment of area for solid wall with no pit chambers present
I_h	l^4	second moment of area for median section through single pit
K_{sc}	$l^2 \cdot t \cdot p^{-1}$	conduit conductivity per length and per wall area
K_{sp}	$l \cdot t \cdot p^{-1}$	pit conductivity per membrane area
n_s	—	number of radial microfibril spokes in membrane
n_{po}	—	number of pores in membrane
n_{pi}	—	number of pits in tracheid
n_{pi}'	—	number of pits in one row of opposite pitting
L_e	—	ligament efficiency
P_y	p	pressure across membrane at deflection y
P_c	p	capillary-seed pressure
P_i	p	implosion pressure
P_r	p	rupture-seed pressure
R	p · t^{-1} · l^{-3}	hydraulic resistance
R_a	p · t^{-1} · l^{-3}	hydraulic resistance of single pit aperture
R_c	p · t^{-1} · l^{-3}	hydraulic resistance of vessel
R_l	p · t^{-1} · l^{-3}	hydraulic resistance of vessel lumen
R_m	p · t^{-1} · l^{-3}	hydraulic resistance of pit membrane
R_p	p · t^{-1} · l^{-3}	hydraulic resistance of pit
R_w	p · t^{-1} · l^{-3}	hydraulic resistance of vessel wall
r_{ya}	l	radius of curvature of pit chamber wall
r_y	l	radius of curvature of membrane at deflection y
s	l	distance between pit edges for opposite pitting arrangement
t_a	—	pit aperture length
V_a	l^3	pit aperture volume
V_c	l^3	pit chamber volume (to one side of membrane)
V_s	l^3	conduit wall volume if no pits were present
V_t	l^3	conduit wall volume minus pit spaces
y	l	deflection of membrane center from flat position
y_l	l	distance from flat membrane to inner edge of aperture
y_a	l	minimum deflection of membrane at aspiration
Θ	degree	angle of membrane deflection

tensile force vector in each radial spoke that is directed normal to the membrane:

$$\text{resisting force} = n_s T \sin\Theta \quad (6)$$

where n_s is the number of radial spokes, T is the tensile force in each spoke, and Θ is the angle of membrane deflection from the flat position (Fig. 1D). The tensile force is in turn equal to:

$$T = EeA_f \quad (7)$$

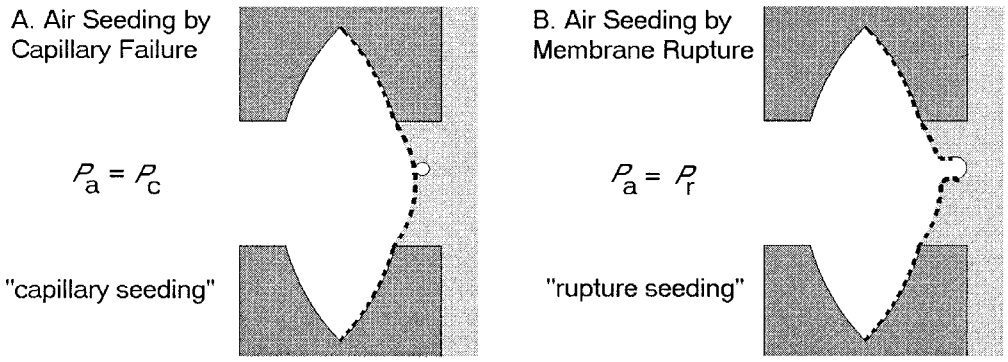

Fig. 2. Modes of air-seeding in angiosperm vessels. Air-seeding occurs when the pressure difference (P_a) between air (left) and water (right) across the pit membrane is high enough to force air through to nucleate cavitation. (A) Air-seeding by capillary failure ("capillary-seeding") occurs when the air-water meniscus fails at preexisting pores in the pit membrane. The P_a thus equals the pressure required to displace such a meniscus (P_c). (B) Air-seeding by membrane rupture ("rupture-seeding") occurs when new holes open up in the membrane owing to its structural failure. The P_a equals the pressure causing the membrane to fail (P_r).

where E is the modulus of elasticity of the spokes, e is their strain, and A_f is their cross-sectional area (we used A_f = 707 nm^2 from Petty, 1972). As reported in the results section, we performed a sensitivity analysis to arrive at provisional settings for E and the microfibril strength, F.

Combining Eqs. 5–7 gives the pressure difference (P_y) required to deflect the membrane a distance y from its unstressed flat position (Fig. 1D):

$$P_y = 2n_s E e_y A_f/(\pi D_m r_y) \quad (8)$$

where the subscript "y" denotes a value at displacement y, and r is the radius of curvature of the membrane (Fig. 1C). This equation makes the simplifying approximation that the membrane curvature is spherical, allowing $D_m/2r_y$ to be substituted for sin Θ. Continuing with the assumption of circular membrane curvature, r_y equates to

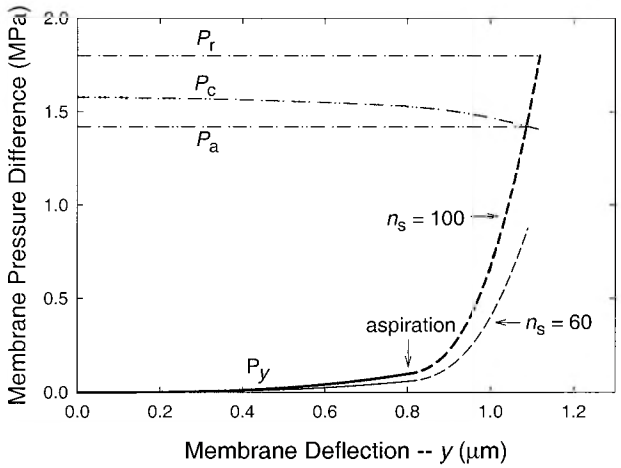

Fig. 3. Pressure difference across pit membrane vs. membrane deflection (y) illustrating how the model computed air-seed pressure. Heavy P_y curve shows pressure required to displace membrane of n_s = 100 spokes by distance y from its flat position. Solid portion of curve is before membrane aspiration, dashed portion of curve is after aspiration. Dash-dotted lines show the capillary-seed pressure (P_c), rupture-seeding pressure (P_r), and air-seed pressure (P_a) for the n_s = 100 pit. This pit air-seeded by capillary failure (P_a = 1.4 MPa) because P_y reached P_c before P_r. The light P_y curve is for a membrane of n_s = 60 spokes; the fewer the spokes the lower the air-seed pressure (P_a = 0.8 MPa). A given air-seed pressure was achieved in the model by iterating the spoke number until the calculated P_a reached the desired value.

$$r_y = (y^2 + D_m^2/4)/(2y) \quad (9)$$

and e_y is

$$e_y = (2\alpha_y r_y/D_m) - 1 \quad (10)$$

where α_y = Acos$[(r_y - y)/r_y]$. By incrementing y and solving for P_y, a pressure vs. displacement relationship can be found (Fig. 3, solid P_y line). When the membrane reached the pit chamber wall, aspiration occurs (Fig. 3, arrow). The y at aspiration (y_a, Fig. 1D) was calculated from a membrane strain at aspiration e_a = 0.03, as estimated from the measurement of several published micrographs of circular bordered pits of different sizes (Panshin and de Zeeuw, 1970; Siau, 1971; Bauch et al., 1972; Core et al., 1979; Siau et al., 1984). This calculation assumed a constant radius of curvature of the inner chamber wall of r_{ya} (Fig. 1C), which was solved numerically from the equality (derived from Eqs. 9 and 10):

$$r_{ya} = D_m/[2\sin(D_m(1 + e_a)/2r_{ya})]. \quad (11)$$

For deflection beyond aspiration (Fig. 3, heavy dashed line), Eq. 8 was modified to account for the deflection of the membrane through the pit aperture:

$$P_y = P_{asp} + 2n_s \Delta e_y E A_f/(\pi r_y D_a) \quad (12)$$

where P_{asp} is the pressure causing aspiration, D_a is the aperture diameter, r is the radius of curvature of the membrane deflecting through the aperture, and Δe is the additional strain caused by deflection through the aperture. This strain was calculated assuming that the stretch across the aperture after aspiration was distributed throughout the entire length of the microfibril spokes.

Equations 8 and 12 were used to generate a P_y vs. y relationship for the pit membrane (Fig. 3). This curve allowed us to predict the air-seed pressure based on which limiting pressure came first during membrane deflection: the rupture-seed pressure (P_r) or the capillary-seed pressure (P_c). The P_r was equal to the P_y where spoke stress (T/A_f) equaled the spoke strength (F). In the example in Fig. 3, P_r is equal to 1.8 MPa (Fig. 3, dash-dotted P_r line). The P_c was given by the capillary equation:

$$P_c = 4\tau\cos(a)/D_p' \quad (13)$$

where τ is the surface tension of water, a is the contact angle between meniscus and wall, and D_p' is the *stretched* diameter

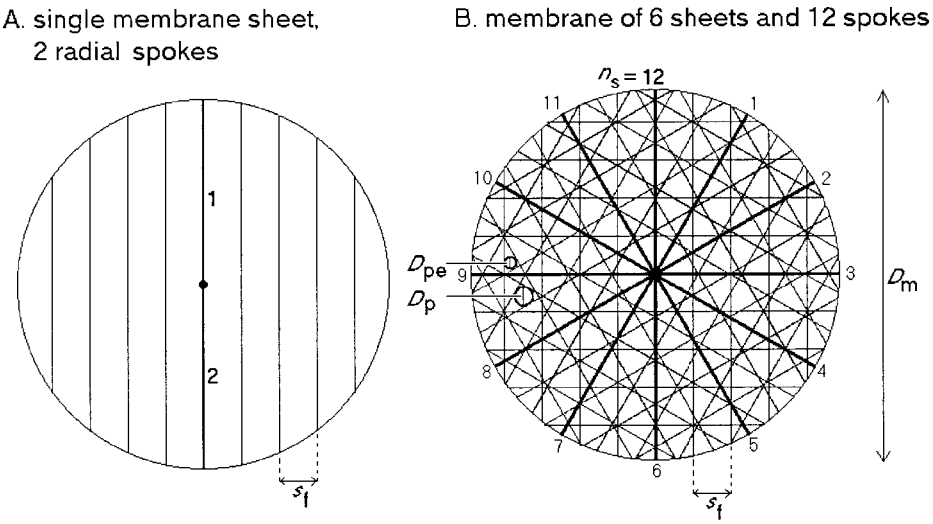

Fig. 4. Representation of pit membrane. (A) A single sheet of parallel microfibrils, each spaced distance s_f apart. One strand from each sheet formed a pair of radial spokes (numbered heavy line) assumed to bear the load on the stressed membrane. (B) A membrane composed of six sheets and n_s = 12 radial spokes (numbered heavy lines). D_p = maximum pore diameter; D_{pe} = equivalent pore diameter giving same membrane conductivity if all pores were of equal size; D_m = membrane diameter; s_f = spacing between strands of a single sheet.

of the membrane pores. The stretching of the pores during membrane deflection caused a decrease in P_c with increasing deflection y (Fig. 3, dash-dotted P_c curve). For the pit membrane in Fig. 3, the P_a was 1.42 MPa (dash-dotted P_a line), and air-seeding occurred by capillary seeding because the deflection pressure reached P_c before P_r.

Membrane structure—To be able to predict D_p' and also the membrane hydraulic conductivity, we needed to link the number of load-bearing microfibril spokes to membrane porosity. This required making several assumptions about membrane structure (Fig. 4): (a) the membrane was made up of several sheets of microfibrils superimposed on one another (Fig. 4B); (b) each sheet consisted of parallel microfibrils spaced a constant distance s_f apart (Fig. 4A); (c) one fibril of each sheet ran across the center of the membrane, forming a pair of microfibril spokes (oriented 180° from each other), so that n_s = twice the number of sheets composing the membrane (Fig. 4A); (d) the angle between adjacent radial microfibrils was 180° divided by the number of sheets in the membrane, or 360°/n_s (Fig. 4B).

These assumptions at least qualitatively reflect cell wall development, given that microfibrils are laid down in multiple layers, and these layers can be composed of roughly parallel microfibrils, and successive layers can cross each other at various angles (Carpita and Gibeaut, 1993). Beyond this similarity to membrane development, the main purpose of these assumptions was to provide a quantitative link between membrane strength, which depended on the number of radial spokes (n_s), and the membrane porosity.

Based on measurements from eight membranes of n_s = 4 to 24, the diameter of the largest circular pore (D_p) inscribed between microfibrils (Fig. 4B) was approximately:

$$D_p \approx 2s_f \sin[180/(n_s + 2)]. \quad (14)$$

The stretched pore diameter (D_p') at each membrane deflection y was calculated assuming that membrane stretch was accounted for by expansion of pores without any shrinkage of microfibril thickness. The approximation in Eq. 14 was of less concern than its main purpose of establishing a consistent quantitative link between membrane strength and porosity.

To set s_f, the spacing between microfibrils of a membrane sheet (Fig. 4), we used Petty's measurements from conifer membranes where the porous structure of the margo allows both D_p and n_s to be measured. Petty (1972) reported that a pore size of approximately 0.1 μm corresponded with an n_s of approximately 100. From Eq. 14, this gives an s_f of approximately 1.5 μm. This s_f setting was used as the default for angiosperm and conifer membranes alike to simplify the comparison between pit types. Variation in membrane porosity was thus achieved by varying the number of microfibril sheets rather than the spacing within a sheet. As noted in the results section, we assessed the effect of varying the s_f setting from the default over a range from 0.5 to 3.0 μm.

To match a given membrane structure with a specific air-seed pressure, we increased the number of spokes (n_s) by increments of two (two spokes per microfibril sheet; Fig. 4A) and calculated the air-seed pressure for each spoke setting until the desired air-seed pressure was reached. For example, in Fig. 3 a spoke number of n_s = 60 gave an air-seed pressure of 0.88 MPa (light P_y curve, n_s = 60). If the target air-seed pressure was 1.4 MPa, n_s for this same pit would have to be incremented to 100 (heavy P_y curve, n_s = 100).

Pit and conduit hydraulic conductivity—Calculating the hydraulic conductivity of a single pit began with the equation for hydraulic resistance (R, reciprocal of conductance) of a circular pore of diameter D_p in an infinitely thin plate (Vogel, 1994):

$$R = 24\upsilon/D_p^3 \quad (15)$$

where υ is viscosity. If the membrane is assumed to have circular pores of equal diameter and to have negligible thickness, the total membrane conductance could be estimated as the sum of the individual pore conductances. However, closely spaced pores interact such that their individual conductances are greater than predicted from Eq. 15. Tio and Sadhal (1994) have modeled this effect and found that the pore resistance is de-

creased by a fraction equal to the following function of the proportion of the plate area occupied by pores (h):

$$f(h) = 1 - 0.89h^{1.5} - 0.11h^{2.5} - 0.066h^{3.5} - 0.048h^{4.5}. \quad (16)$$

Using this expression for R_m gives the following:

$$R_m = [24\upsilon/(n_{po}D_p^3)]f(h) \quad (17)$$

where n_{po} is the number of pores in the membrane.

The pores in the membrane were not of uniform size nor were they circular (Fig. 4B). To simplify the use of Eq. 17, we estimated the equivalent pore diameter (D_{pe}; Fig. 4B) that gave the same membrane conductivity for the same number of pores as in the actual membrane. We assumed that pores were the largest circle fitting within the membrane openings and that membrane conductivity was proportional to the sum of the pore diameters to the third power (Eq. 17). Based on measurements from the same set of eight membranes used to estimate the maximum pore diameter D_p (Eq. 14), the equivalent pore diameter was approximately 63% of D_p for $n_s > 6$ (always the case):

$$D_{pe} \approx 0.63D_p. \quad (18)$$

The pore number (n_{po}) was estimated from the total membrane area divided by the area of a single circular pore including the surrounding microfibril strand (t_f = 30 nm; Petty, 1972):

$$n_{po} = D_m^2/(D_{pe} + t_f)^2. \quad (19)$$

The D_{pe} and n_{po} from Eqs. 18–19 were used in Eq. 17 to estimate the membrane resistance.

The hydraulic resistance of the pit aperture (R_a) could not be estimated from Eq. 15 because the aperture cannot be regarded as being infinitely short in length. Dagan et al. (1982) provide an approximate solution for the hydraulic resistance of circular pores of finite length that combines Eq. 15 with the Hagen-Poiseuille equation:

$$R_a = 128t_a\upsilon/(\pi D_a^4) + 24\upsilon/D_a^3 \quad (20)$$

where t_a is the length of one aperture (Fig. 1C). We used Eq. 20 to calculate the R_a for the cavitation data set, calculating t_a from the double wall thickness (t_w):

$$t_a = (t_w/2) - (y_1) \quad (21)$$

where y_1 was the distance from the inner aperture edge to the membrane at zero deflection (Fig. 1D). The y_1 was calculated from radius of curvature of the chamber wall (r_{ya}; Eq. 11).

The total pit resistance (R_p) was equal to R_a and R_m in series, ignoring the resistance of the pit chamber:

$$R_p = 2R_a + R_m. \quad (22)$$

To represent the hydraulic efficiency of individual pits, we converted the pit resistance to a conductance per membrane area (pit $K_{sp} = 4/(R_p\pi D_m^2)$).

The accuracy of Eqs. 17, 20, and 22 was tested by applying them to physical models of pits with well-characterized shape, pore sizes, and aperture configurations (Lancashire and Ennos, 2002). The agreement with measured values was extremely close (Fig. 5), suggesting that the largest source of error will be the estimates of pore size and number in Eqs. 18 and 19.

To calculate the total vessel resistance (R_c), we followed the method of Lancashire and Ennos (2002):

$$R_c = R_l + R_w \quad (23)$$

where R_l is the contribution of the conduit lumen and R_w the contribution of the conduit wall pitting to the total conduit resistance. The R_l is the Hagen-Poiseuille resistance of the lumen for half of the conduit length, because water on average traverses just half of a conduit's total length:

$$R_l = 64\upsilon L/(\pi D_c^4) \quad (24)$$

where L is the total length of the vessel.

Similarly, R_w is the parallel resistance of just half of the vessel's pits:

$$R_w = 2R_p/n_{pi}. \quad (25)$$

The number of pits per vessel (n_{pi}) was given by

$$n_{pi} = \text{int}[LX/(D_m + s)]\, n_{pi}' \quad (26)$$

where int[number] returns the largest integer less than or equal to the number and LX is the cumulative length of pitted walls, with the "pitting coefficient" X being the proportionality factor between the vessel length and the cumulative pitted length. For example, if a vessel had pitted walls on two sides for all of its length, X = 2. Vessel length (L) and pitting coefficient (X) were not measured, and we present a sensitivity analysis of these variables in the results. Equation 26 makes the simplifying assumption that the minimum vertical spacing between horizontal rows of pits equals the minimum spacing within a single row. The n_{pi}' term in Eq. 26 is the number of pits fitting side-by-side across the conduit wall of width b in an opposite pitting arrangement (Fig. 1):

$$n_{pi}' = \text{int}(b/D_m). \quad (27)$$

The R_c is the resistance of a vessel—the hydraulic pressure drop across the vessel divided by the flow rate. To assess the hydraulic efficiency of a conduit, we expressed the hydraulic conductance of a single vessel on a per-conduit length and per-unit cross-sectional wall area basis (K_{sc}):

$$K_{sc} = L/(R_c A_w) \quad (28)$$

where A_w is the cross-sectional area of the wall of a single conduit. To account for the wall investment in the conduit over its entire length, the A_w was calculated from the total wall

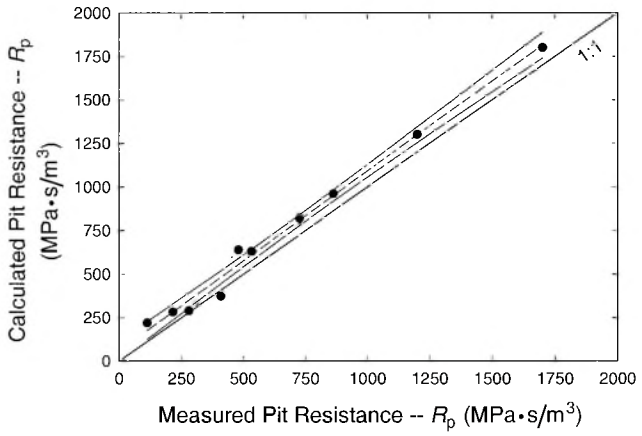

Fig. 5. Measured vs. calculated hydraulic resistance of physical models of circular bordered pits (R_p). Measured values are from Ennos and Lancashire (2002). Calculated values are from Eqs. 17, 20, and 22 based on the pit model dimensions. Aperture length (t_a) was not reported, but the aperture was constructed from a hose gasket, so assumed t_a = 2 mm. This is equivalent to t_a = 1.1 μm according to the scale factor of 1830.

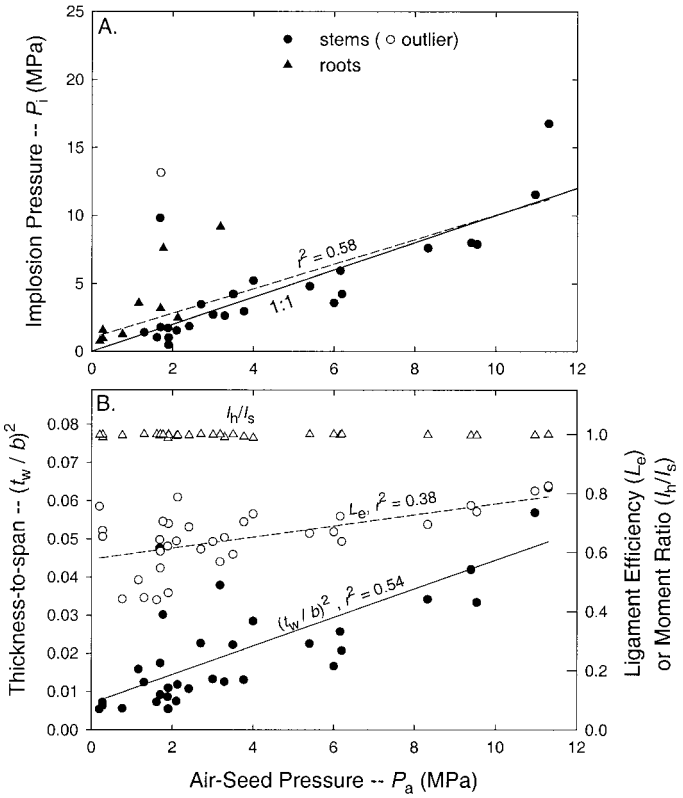

Fig. 6. (A) Implosion pressure (P_i) vs. air-seed pressure (P_a) for xylem samples in the data set. Symbols are measured values, dashed line is regression through data excluding one outlier (open circle, >3 standardized residuals from mean), and solid line is 1 : 1. (B) Components of implosion pressure vs. air-seed pressure. Left ordinate and solid symbols is the thickness-to-span ratio $(t_w/b)^2$. Right ordinate is the ligament efficiency (L_e; open circles) or the moment ratio (I_h/I_s; open triangles).

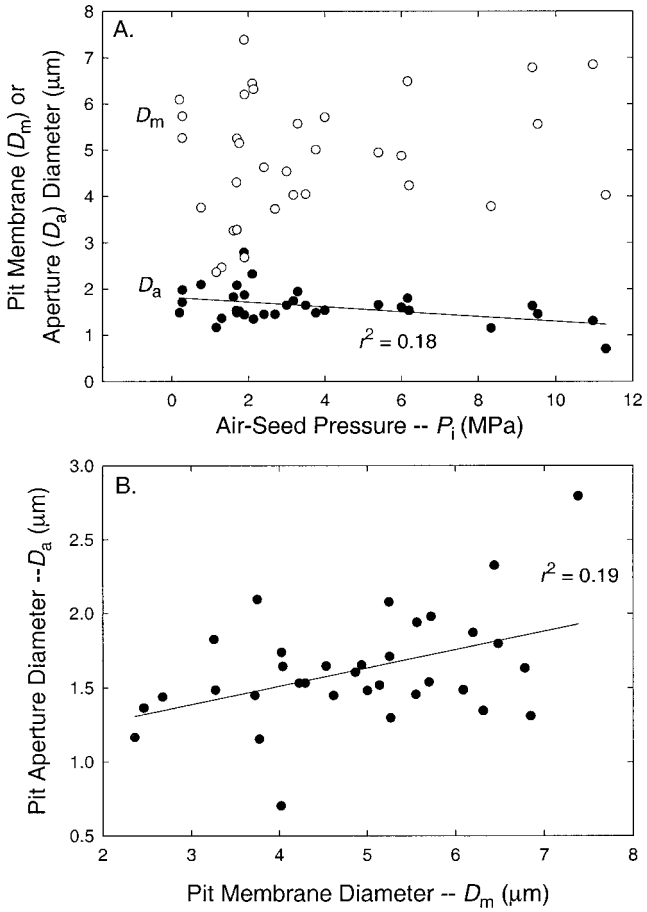

Fig. 7. (A) Pit aperture diameter (D_a; solid circles) and membrane diameter (D_m; open circles) vs. air-seed pressure for data set. (B) Pit aperture diameter vs. pit membrane diameter.

volume of the conduit (V_t) divided by the conduit length ($A_w = V_h/L$). The V_t was

$$V_t = V_s - n_{pi}(V_c + V_a) \quad (29)$$

where V_s is the volume of the wall assuming no pits, V_c is the volume of one pit chamber, and V_a the volume of one pit aperture. Volume components were computed as:

$$V_s = [(D_c + t_w)^2 - D_c^2]L \quad (30)$$

$$V_c = \pi[y_a^2(r_{ya} - y_a/3) - (y_a - y_1)^2(r_{ya} - (y_a - y_1)/3)] \quad (31)$$

$$V_a = \pi D_a^2 t_a/4. \quad (32)$$

This wall volume estimate assumed a square conduit with sides equal to D_c. This was an approximation, as would be an estimate based on a cylindrical geometry or any other regular shape. It was acceptable, however, because the most important objective was to establish a consistent proportionality between conduit volume and length.

RESULTS

Wall implosion pressure (P_i) and conduit dimensions—The conduit implosion pressure was positively correlated with the measured air-seed pressure with an average safety factor (P_i/P_a) greater than 1 as predicted (Fig. 6A). The stem and root regressions were not significantly different in slope or intercept and were pooled. From the regression line ($P_i = 0.90P_a + 1.0$), the safety factor from implosion ranged from 2.1 at $P_a = 1$ MPa to 1.0 at $P_a = 10$ MPa, with an average of $P_i/P_a = 1.8$. One outlier (*Laurus nobilis*) had an implosion pressure more than three standardized residuals greater than the mean (Fig. 6A, open symbol).

The increase in implosion pressure with air-seed pressure was mostly the result of increased thickness-to-span ratio $(t_w/b)^2$, which was correlated with air-seed pressure (Fig. 6B, solid symbols). Neither of the two components of thickness-to-span ratio, b or t_w, were correlated with air-seed pressure, just their ratio. The ligament efficiency (L_e) also increased with air-seed pressure, but to a lesser extent (Fig. 6B, open circles). The moment ratio (I_h/I_s) was essentially equal to one for all pits (Fig. 6B, open triangles), meaning that the presence of a pit chamber did not significantly weaken the wall. Thus, the weakening of the wall by pits was entirely due to the apertures and was accounted for by the ligament efficiency. Based on the L_e range of approximately 0.6–0.8, pits weakened the wall by 20–40% relative to a solid wall of the same dimensions with no pits.

For most species, the spacing between pits in the vessel wall (s, Eq. 2) was negligible, meaning that the L_e was approximated by $1 - D_a/D_m$. The increase in L_e with air-seed pressure was primarily a result of a decrease in D_a (Fig. 7A, solid symbols) rather than any increase in D_m with air-seed pressure

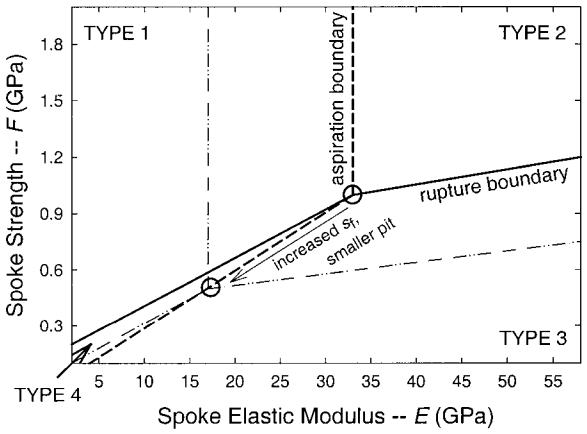

Fig. 8. Influence of microfibril spoke strength (F) and elastic modulus (E) on pit aspiration and mode of air-seeding. Pits were of average D_m (4.9 μm), D_a (1.6 μm), and air-seed pressure (P_a = 3.6 MPa). Type 1 pits capillary-seeded after aspiration. Type 2 pits capillary-seeded without aspiration. Type 3 pits rupture-seeded without aspiration. Type 4 pits rupture-seeded after aspiration. The solid "rupture boundary" divides rupture-seeding pits (below) from capillary-seeding pits (above). The dashed "aspiration boundary" divides aspirating pits (above and to left) from nonaspirating pits (below and to right). Decreasing the pit size, or increasing the microfibril spacing, caused the circled four-way intersection between pit types to move down the aspiration diagonal (arrow); and vice versa. The dotted lines show the boundary shift associated with increasing s_f to 3.0 μm from the default of 1.5.

(Fig. 7A, open symbols). Although pit membranes varied from a D_m of 2.4–7.5 μm, the D_a was correlated with D_m (Fig. 7B), keeping L_e relatively constant with pit size.

The scaling of vessel and pit dimensions allowed us to define what is hereafter referred to as the "average" vessel for the data set. This vessel had the average hydraulic diameter for the data set of D_c = 49 μm and the average air-seed pressure of P_a = 3.6 MPa. The corresponding implosion pressure was 4.24 MPa from the regression in Fig. 6A, and the thickness-to-span ratio was 0.02 from the regression in Fig. 6B; the D_a was 1.6 μm from the regression in Fig. 7A, and the D_m was the mean of 4.9 μm from the data set.

Mode of air-seeding and the mechanical properties of membrane microfibrils (E, F)—Whether or not a pit rupture-seeded or capillary-seeded and whether pits aspirated or not before seeding depended on the strength (F) and elastic modulus (E) of the radial microfibril-based spokes (Fig. 8). The ambiguity of spoke structure—whether the spokes are continuous microfibrils or aggregates of overlapping ones—made it difficult to assign F and E values. For individual cellulose microfibrils, estimates of F range from an upper limit of 25 GPa to a lower value near 1 GPa and E ranges from 250 to 3 GPa (Mark, 1967; Petty, 1972; Jeronimidis, 1980; Ashby et al., 1995; Hepworth and Vincent, 1998a, b). Estimates for F and E of primary cell walls fall within the lower end of this range and below (Vincent, 1999).

In lieu of more direct information, we conducted an extensive sensitivity analysis across the range of likely F and E for pits of the average vessel. All four possible combinations of seeding and aspiration were observed (Fig. 8).

Type 1 pits showed aspiration and capillary-seeding. These pits had high F and low E—strong, flexible membranes (Fig. 8, upper left).

Type 2 pits showed no aspiration and capillary-seeding. These were associated with high F and high E—strong, stiff membranes (Fig. 8, upper right).

Type 3 pits showed no aspiration and rupture-seeding. These were associated with relatively low F and high E—weak, stiff membranes (Fig. 8, lower right).

Type 4 pits showed aspiration and rupture-seeding. These pits occupied a thin wedge between type 1 and 3 pits (Fig. 8).

The boundaries between pit types were essentially independent of the air-seed pressure. Although increasing the air-seed pressure increased the force on the pit membrane, it also required an increase in the number of sheets making up the membrane and hence, an increase in the number of load-bearing microfibril spokes. The result was that the force per spoke at air-seeding did not vary substantially, keeping the boundaries between pit types relatively constant.

The boundaries between pit types did depend on the aspiration strain (e_{ya}), pit size, and the choice of microfibril spacing, s_f. The aspiration strain setting of e_{ya} = 0.03 demarcated the diagonal portion of the "aspiration boundary" (Fig. 8, dashed line). The ratio F/E is the membrane strain at rupture and so no pit could aspirate without rupturing first at an F/E below 0.03. The vertical portion of the aspiration boundary was set by the E threshold above which aspiration could not occur because it was preceded by capillary seeding.

Decreasing the pit size (while maintaining observed scaling between D_a and D_m; Fig. 7B) or increasing the microfibril spacing (s_f) shifted the four-way intersection of pit types (Fig. 8, circled point) to a lower point on the F/E = 0.03 diagonal (Fig. 8, arrow showing shift for s_f changed from 1.5 to 3 μm). This reduced the range of type 1 and type 4 pits (Fig. 8, dot-dash boundaries between pit types). In both cases, the force per spoke at air-seeding was reduced, meaning that aspiration occurred for a smaller range of E. A small membrane size reduced the force on each spoke according to Eq. 5, and a higher s_f required more membrane sheets (and hence, spokes) to achieve the same membrane porosity, leading to less force per spoke.

Assuming that pits aspirate prior to air-seeding, in agreement with limited observations (Petty, 1972; Thomas, 1972), the F and E must lie within the aspiration boundary that includes both type 1 and type 4 pits (Fig. 8). Making the further assumption that pits do not rupture-seed, given that this could cause irreparable damage to the membrane, we can narrow down the F and E values further as those leading to type 1 pits. From the boundary between type 1 and 4 pits this means F/E must exceed approximately 0.1. Except where noted, the default setting for all subsequent analyses was F = 2.2 and E = 5 GPa, which was substantially within the type 1 domain for all pit dimensions.

Pit conductivity (pit K_{sp}) vs. air-seed pressure (P_a)—The model predicted a significant decline in pit K_{sp} with increasing P_a (Fig. 9A, r^2 = 0.88). Pit K_{sp} dropped by a factor of 30 for a 10-fold increase in P_a from 1 to 10 MPa. These calculations were for pits and vessels of measured diameters and of a wall thickness giving the P_i predicted from the regression in Fig. 6A.

The decline in K_{sp} with P_a was attributable to both a drop in membrane conductivity and aperture conductivity (Fig. 9B). Membrane conductivity per membrane area declined in a regular manner (Fig. 9B, solid symbols) as a result of the smaller membrane pores and higher microfibril densities required to capillary-seed at a higher P_a. Aperture conductivity per mem-

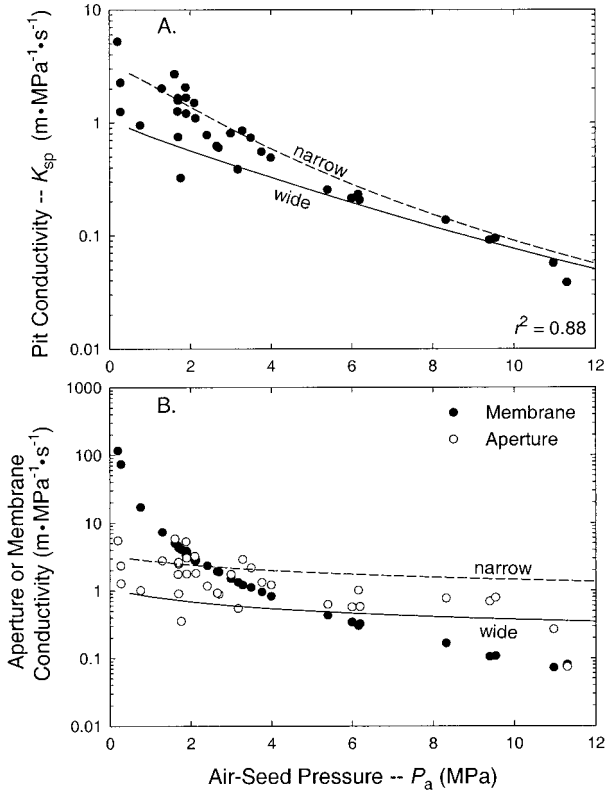

Fig. 9. (A) Pit conductivity per membrane area (pit K_{sp}) vs. air-seed pressure (P_a). Solid symbols represent pits of measured dimensions from the data set. Dashed line ("narrow") is for pits of average dimension in a conduit of minimum diameter (D_c = 23 μm); solid line ("wide") is for pits of average dimension in a conduit of maximum diameter (D_c = 102 μm). The r^2 for the regression was 0.88. (B) Components of pit K_{sp} vs. air-seed pressure. Solid circles represent membrane conductivity per membrane area; open circles show aperture conductivity per membrane area for pits of measured dimensions. Dashed ("narrow") and solid ("wide") lines represent the aperture conductivities for narrowest and widest vessels in the data set as in panel (A).

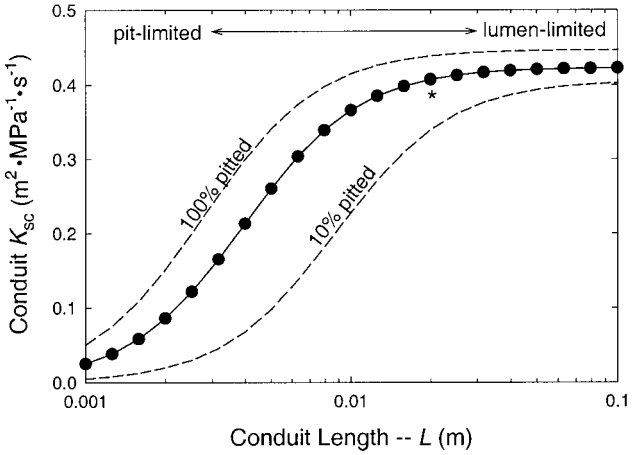

Fig. 10. Vessel conductivity per length and per wall area (K_{sc}) vs. vessel length (L) for the average vessel (see text). Symbols represent vessels with pitting on 50% of their wall area (X = 2, Eq. 26). Dashed lines indicate 10% and 100% pitting as indicated. Short vessels had low K_{sc} determined by the dominating influence of pit resistance. In long vessels, the relative contribution of pit resistance diminished, and the K_{sc} saturated at a maximum value determined by the conductivity of the lumen and the transverse wall area. The "saturating vessel length" was the length required to achieve 95% of the maximum K_{sc} (asterisked point for 50% pitting; L = 0.02 m).

brane area also declined (Fig. 9B, open symbols) because of the thicker walls (and hence larger aperture depth t_a) required to keep P_i equal to P_a, and because of the slight decline in aperture diameter with increasing P_a (Fig. 7A). For P_a below approximately 2 MPa, aperture conductivity was less than membrane conductivity, and so was the limiting factor for the overall pit conductivity. Above approximately 4 MPa, the membrane conductivity became limiting.

The scatter in the aperture conductivities was a result of the variation in conduit diameter (D_c). A higher D_c required a thicker wall to maintain a given implosion pressure and hence a lower aperture conductivity. As a result, the wider the conduit, the lower the pit conductivity. This effect is illustrated by the "wide" vs. "narrow" curves for aperture conductivity (Fig. 9B) and pit conductivity (Fig. 9A). These curves were calculated for the widest (102 μm) and narrowest (23 μm) conduits in the data set (using average pit dimensions). This disadvantage of wider conduits had the most influence on pit K_{sp} at low P_a (Fig. 9A) where aperture conductivity was lower than membrane conductivity (Fig. 9B) and hence more limiting. Thus, although a wider conduit has a much greater lumen conductivity according to the Hagen-Poiseuille equation, its pits are necessarily less efficient conductors on a per-membrane-area basis.

Pit conductivity predictions were insensitive to F as long as these settings allowed type 1 pits. This was because membrane strength does not determine the air-seed pressure for capillary-seeding pits. Pit conductivity declined slightly with increasing E, because more microfibrils were needed to compensate for greater stretch. The more microfibrils, the narrower the pores and the lower the conductivity of the relaxed membrane. This effect was rather minor, however, resulting in a 13% decline in average pit K_{sp} for an 80% reduction in E (from 5 to 1 GPa).

Pit conductivities were insensitive to the spacing of microfibrils in a membrane sheet (s_f) for type 1 pits. Changing the s_f from the default of 1.5 μm to 0.5 or 3.0 μm only altered the number of membrane sheets and radial spokes required to obtain an air-seed pressure; the membrane porosity and thus conductivity was essentially constant regardless of s_f.

Vessel conductivity (K_{sc}) vs. air-seed pressure—The conducting unit in angiosperm xylem is not one pit but the vessel that consists of multiple pits in series with the vessel lumen. The vessel K_{sc} reflects the contribution of pit and lumen components to the hydraulic conductivity of a single conduit. The hydraulic conductivity was expressed per conduit wall area per unit length. A greater vessel K_{sc} means the plant can move more water with less drop in water potential per unit length and less investment in wall material per unit length.

To calculate vessel K_{sc} we needed to know the conduit length (L) and the "pitting coefficient," X, which determined the cumulative length of pitted wall (FX; Eq. 26). Neither parameter was measured, and we present a sensitivity analysis in which all other parameters were constant at values for the average vessel.

The vessel K_{sc} increased in sigmoidal fashion with L (Fig. 10). Short conduits had low K_{sc} because their conductivity was dominated by the pits with their narrow channels and high resistance to flow (Fig. 10, "pit-limited"). Long conduits had higher K_{sc} because their conductivity was dominated by the

conduit lumen with its very low resistance to flow (Fig. 10, "lumen-limited"). At a certain length, the vessel K_{sc} became saturated at a value set by the Hagen-Poiseuille conductivity of the lumen and the cross-sectional area of the conduit wall. This "saturated vessel K_{sc}" was calculated directly from the model, but its dependence on conduit diameter and wall thickness can be represented in simplified form:

$$\text{saturated vessel } K_{sc} \propto D_c^4/[(t_w + D_c)^2 - D_c^2] \qquad (33)$$

where the proportionality depends in part on the volume of the pits.

We defined a "saturating vessel length" as the length required to achieve 95% of the saturated vessel K_{sc}. Intuitively, the saturating length should be the optimal vessel length because shorter vessels are not as conductive, and longer vessels contribute little to conductivity when functional yet cause a greater loss of conductivity when cavitated (Comstock and Sperry, 2000).

The saturating vessel length depended on how much of the wall was occupied by pits, as determined by the pitting coefficient, X. The maximum X was 4 when all vessel walls were pitted over their entire length (100% pitting). The higher the pitting percentage, the higher was the pit conductivity, and the shorter the vessel length required to saturate the K_{sc} (Fig. 10; 100% pitting line, $X = 4$). The lower the pitting percentage, the more limiting was the pit conductivity, and the longer the vessels had to be to maximize K_{sc} (Fig. 10; 10% pitting line, $X = 0.4$). For the average vessel, a 50% pitting percentage ($X = 2$) corresponded with a saturating vessel length of 2 cm (Fig. 10, asterisk). The 50% pitting percentage was adopted as the default for subsequent analyses.

The saturating vessel length also depended on the vessel diameter (Fig. 11A). The wider the vessel, the higher the lumen conductivity, and the greater must be the length for lumen conductivity to become limiting. Saturating lengths varied from 2.3 mm for $D_c = 20$ μm to 4.4 cm for $D_c = 100$ μm (Fig. 11A, solid line). While these may seem like short vessel lengths, they compare favorably to measurements of median hydraulic diameter (smallest diameter class achieving 50% or more of the cumulative Hagen-Poiseuille conductivity) vs. median vessel length from previous work on woody temperate trees and shrubs, including some of the same species used in the present study (Fig. 11A, open symbols). These species were: *Alnus crispa*, *A. incana*, *Populus tremuloides*, *Betula occidentalis*, *B. papyrifera*, *Artemisia tridentata*, *Acer rubrum*, and *Quercus gambelii* (Zimmermann and Potter, 1982; Sperry and Sullivan, 1992; Sperry et al., 1994; Kolb and Sperry, 1999a). Medians were used because vessel length distributions are strongly skewed to shorter length classes (Zimmermann and Jeje, 1981). An exception was made for *A. rubrum* for which only mean vessel diameter was reported (Zimmermann and Potter, 1982).

Finally, the saturating vessel length also depended on the air-seed pressure. A higher air-seed pressure corresponded to a lower pit conductivity (Fig. 9A). A lower pit conductivity required a longer lumen to overcome the pit limitation and reach the saturated vessel K_{sc}. This effect caused the variation in the relationship between saturated vessel length and vessel diameter (Fig. 11A).

The saturated vessel K_{sc} increased as a power function of vessel diameter according to Eq. 33 (Fig. 11B). The scatter results from variation in air-seed pressure that was independent of conduit diameter. Air-seed pressure influenced the saturated

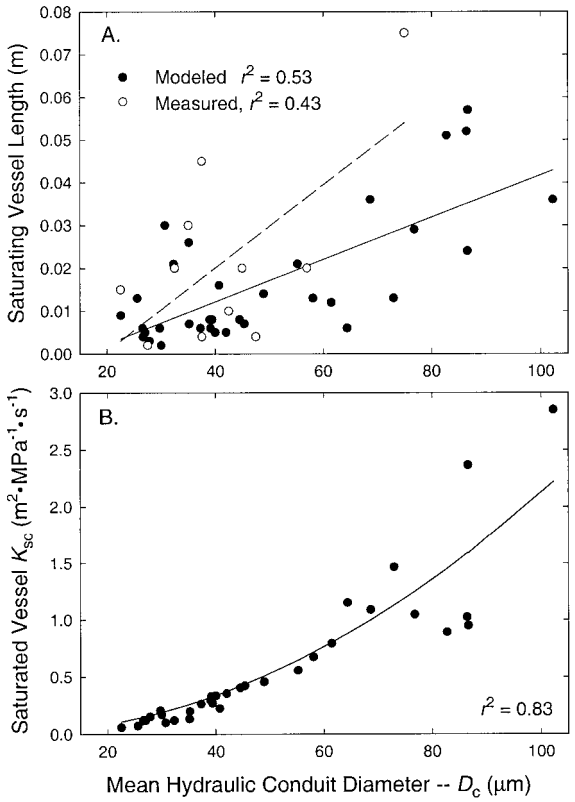

Fig. 11. (A) Saturating vessel length vs. hydraulic mean conduit diameter (D_c) modeled from the data set (solid circles). The median vessel length and corresponding median hydraulic diameter from the literature on temperate woody plants of the same genera (and species, in some cases, Zimmermann and Potter, 1982; Sperry and Sullivan, 1992; Sperry et al., 1994; Kolb and Sperry, 1999a) are shown as open circles. (B) Saturated vessel K_{sc} vs. mean hydraulic conduit diameter (D_c). Curve fit based on Eq. 33.

K_{sc} by changing the wall thickness (t_w) required to maintain the necessary implosion resistance (Eq. 33).

There was a significant negative relationship between the saturated vessel K_{sc} and increasing air-seed pressure, but with considerably more scatter (Fig. 12, $r^2 = 0.33$) than seen for the pit K_{sp} vs. P_a relationship in Fig. 9A ($r^2 = 0.88$). As for pit K_{sp}, the scatter was related to conduit diameter. Unlike the pit K_{sp}, however, wider conduits had much higher vessel K_{sc} than narrow ones (Fig. 12, compare wide vs. narrow lines). Although the pits in wide conduits are *less* conductive (Fig. 9), in long vessels where pit conductivity is less important, this disadvantage is masked by the much greater conductivity of a wide lumen. The scatter results from the fact that vessel diameter was not correlated with air-seed pressure.

The vessel K_{sc} vs. P_a trade-off was also less steep on average than for pit K_{sp}. Whereas pit K_{sp} dropped by a factor of 30 for a 10-fold increase in P_a from 1 to 10 MPa, the vessel K_{sp} dropped by less than a factor of 6. The fact that the vessel conductivity was limited by the lumen rather than the pit component eliminated the effect of the latter. The decline in vessel K_{sc} was not due to a decrease in conduit diameter with P_a, because the two were not correlated. The decline in vessel K_{sc} was solely because of the increase in t_w with P_a as required to maintain implosion pressure.

Maximum possible vessel K_{sc}—Does the observed angiosperm vessel structure provide the greatest possible vessel con-

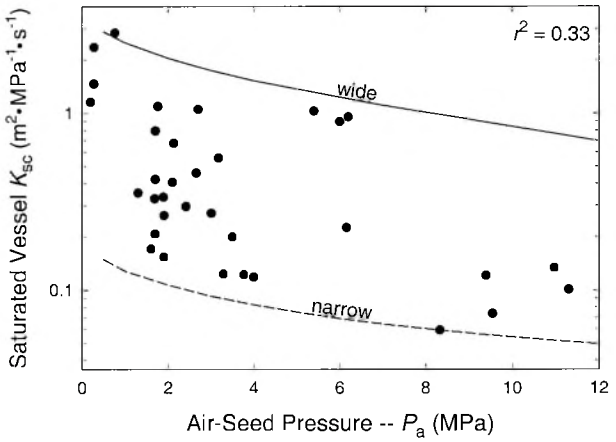

Fig. 12. Saturated vessel conductivity per length and per wall area (K_{sc}) vs. air-seed pressure (P_a) for each xylem sample in the data set. The r^2 for the regression (not shown) was 0.33. The correlation was weak, because vessel diameter was not correlated with P_a. The solid line was for average pit dimensions and the widest vessel diameter (D_c = 102 μm); the dashed line was for average pit dimensions and the narrowest vessel diameter (D_c = 23 μm).

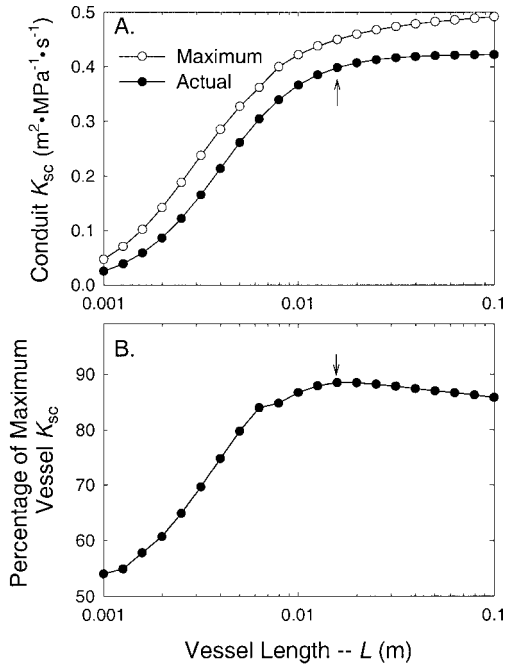

Fig. 13. (A) Vessel conductivity per length and per wall area (K_{sc}) vs. vessel length (L). Solid symbols are for the average vessel and are the same values as in Fig. 10. Open symbols are maximum possible K_{sc} achieved by allowing pit membrane and aperture diameters to vary. (B) The percentage of the maximum possible K_{sc} achieved by actual pits vs. vessel length (L). Actual K_{sc} rose to over 88% of the maximum (arrows in panels [B] and [A]) for vessels near the saturating length for actual pit dimensions.

ductivity per unit investment in wall material and per air-seed pressure? We have already seen that the implosion pressure was only slightly greater than the air-seed pressure on average (Fig. 6A), suggesting that little wall material is invested beyond what is required to prevent conduit implosion. This economy will also enhance the hydraulic conductivity by minimizing the thickness-to-span ratio $(t_w/b)^2$ and the ligament efficiency (L_e). However, a single implosion resistance can be achieved by innumerable combinations of t_w/b and L_e (Eq. 3), and a single L_e can be obtained from many combinations of pit aperture and membrane diameters (Fig. 1B), some of which may pack more pit area per wall area than others. What combination of wall thickness and pitting dimensions gives the maximum vessel K_{sc}? How close is the vessel K_{sc} calculated for the average vessel (Fig. 10) to the maximum possible K_{sc}?

To find the pit structure that maximized vessel K_{sc}, we computed the K_{sc} for a wide range of pit diameters (D_m = 1–20 μm) each with aperture diameters ranging from D_a = 0.2 μm to $D_a = D_m - 0.2$ μm. The wall thickness was allowed to vary to maintain the implosion pressure of the average vessel. All other parameters were also kept at the value for the average vessel. We repeated this analysis for all vessel length settings to find the maximum K_{sc} independently at each length setting (Fig. 13; open symbols).

The maximum vessel K_{sc} exceeded the actual K_{sc} across all settings of vessel length (Fig. 13A, compare open vs. closed symbols). However, the actual K_{sc} rose to within 88% of the maximum at the saturating vessel length (Fig. 13B, arrow). This result suggests that actual pit structure is optimized for vessels near the length-saturating value.

The reason that actual vessel K_{sc} still fell 12% short of the maximum even at the saturating vessel length may have to do with limitations on the size of real pits. Pit dimensions that maximized vessel K_{sc} were larger than what we observed. The optimal D_m at the saturating vessel length was 16.2 μm and D_a was 2.7 μm. The corresponding pit dimensions for the average vessel were D_m = 4.9 and D_a =1.6 μm. Larger pits require a higher F to avoid rupture seeding. Our F setting of 2.2 GPa was high enough to avoid rupture-seeding at all dimensions. If the actual F were low enough, it would limit the maximum pit dimensions possible without rupture-seeding. An F below our setting may explain why optimal dimensions were not achieved in real pits. Large pits were optimal because they resulted in a high ligament efficiency. A high ligament efficiency allowed a thinner wall for the same implosion pressure and hence a greater hydraulic conductivity per wall area (Eq. 33) for vessels at or near their saturated K_{sc}.

DISCUSSION

The results of our analysis allow us to put some provisional numbers on the effect of pits on hydraulic conductivity, conduit wall strength, resistance to cavitation via air-seeding, and vessel length. The analysis of wall strength confirms the long-held assumption that the pit chamber itself does not weaken the wall (Carlquist, 1988) because the moment ratio (I_h/I_s; Fig. 6B) did not differ substantially from 1. The pit apertures, however, do weaken the wall, reducing the implosion pressure by 20–40% based on the observed range of ligament efficiencies (L_e; Fig. 6B). The strengthening of the pitted wall with increasing air-seed pressure was primarily achieved by thickening the wall rather than altering the pitting and ligament efficiency (Fig. 6B). A higher thickness-to-span ratio translates directly into higher wood density, with the result that more cavitation-resistant woods are denser and more expensive to grow than cavitation-susceptible woods. This result generalizes previous observations that vessels from plants of arid habitats tend to have thicker walls (Carlquist, 1988), with the clarification that it is not wall thickness but thickness-to-span ratio that is increasing with aridity.

The strength of pitted vessel walls appears to cut it rather close with implosion pressures being on average only 1.8 times greater than necessary to avoid imploding at the air-seed pressure (Fig. 6A). The advantage of small safety factors is greater economy of conduit construction and greater hydraulic conductivity. Reducing the thickness-to-span ratio $(t_w/b)^2$ of the average vessel by 50% causes a 44% increase in the saturated vessel K_{sc} (Eq. 33). It seems doubtful that the P_i/P_a ratio could be less than one, because an imploding vessel would probably cavitate by air-seeding as the wall began to collapse. This may explain why imploded vessels are rarely observed (Ewers, 1985; Baas, 1986), because the cavitation would eliminate the pressure difference and arrest the implosion. Completely collapsed conduits have been observed in lignin- or cellulose-deficient vessels where the walls are presumably so weak that they fold under very slight negative pressures where cavitation is unlikely (Smart and Amrhein, 1985; Turner and Somerville, 1997; Piquemal et al., 1998).

Recently it has been observed that the tracheids of pine needle collapse prior to cavitation (Cochard et al., 2004). The collapse was reversible and was not initiated by bending stresses as modeled in our analysis. What appears to be a controlled and reversible collapse may be an alternative to cavitation as a means of shutting down water transport and stomatal conductance. It was not observed in stem tracheids (consistent with our analysis) and may be limited to tissues not involved in mechanical support (Cochard et al., 2004). It would seem to also require a very specialized conduit structure that allows for reversible lumen collapse without disruption of walls and vascular connections.

Probably the greatest uncertainties in the wall-strength analysis is the value of the wall strength itself (W) and the effect of the surrounding fibers or tracheids on the vessel wall stress. Wall strength is greater under tension vs. compression, and it is greater in dry wood (where it is usually measured) vs. green wood. Furthermore, it is usually reported on the basis of total wood area, not on a wood cell wall basis. Our value of W = 80 MPa was the tensile strength after conversion from air-dried to saturated moisture content and after correction to a wall-area basis (Hacke et al., 2001a). Overestimating the W will lead to overestimates of P_i/P_a safety factors and vice versa (Eq. 1). As for the effect of fibers, in previous studies the wall density of the fiber matrix was proportional to the wall density of the vessel network (Hacke and Sperry, 2001; Hacke et al., 2001a), suggesting that fiber strength may scale with conduit strength and air-seed pressure. Fibers could probably provide additional strength to the vessels—a factor not accounted for in our analysis.

Much more uncertainty surrounds the mechanical properties of the pit membranes and hence the functioning of pits during air-seeding. In following Petty's (1972) analysis of conifer pit membranes, we have assumed that radial microfibril strands bear the load in the stressed membrane. This is an oversimplification because the load is probably distributed over non-radial strands and the cross-linking matrix between strands. However, regardless of what combination of microfibril and matrix bear the load, the acting and resisting forces on the membrane should still be directed radially. Our radial "spokes" fundamentally represent units of force resistance in the membrane whether or not they consist of single continuous microfibril strands (Fig. 4B). The F and E properties of these radial units dictate whether a pit will aspirate or not and whether air-seeding will occur by capillary-seeding or rupture-seeding (Fig. 8). Our assumption, that pits aspirate and capillary-seed (Fig. 8, type 1 pits), awaits confirmation by empirical measurements of membrane function—a considerable challenge.

Although we intentionally assumed a membrane strength sufficient to avoid rupture-seeding at all pit dimensions, this may not be realistic. The phenomenon of "cavitation fatigue" suggests that membrane strength may be limiting. By analogy with metal fatigue, pit membranes can become weakened by cavitation, air-seeding at a much lower pressure thereafter (Hacke et al., 2001b). Presumably the initial air-seed event was associated with at least limited structural failure, which compromised subsequent sealing capability. The fatigue phenomenon is reversible in at least one species, suggesting that outright rupture of the membrane does not occur (Stiller and Sperry, 2002). The membrane may be stretched beyond the elastic limit, allowing plastic creep and air-seeding without complete parting of the membrane. Supporting this idea is the observation that pit aspiration itself probably induces membrane creep (Petty, 1972). Restoration of the original air-seed pressure requires ingredients in the xylem sap with pH and ionic strength being important (Stiller and Sperry, 2002). Other experiments have shown that oxalic acid and calcium treatments that increase membrane flexibility also dramatically reduce the air-seed pressure, again suggesting membrane mechanical properties may be limiting to pit function (Sperry and Tyree, 1988). If pit membranes are weak enough in reality, pit diameters may not be able to achieve the large size (e.g., D_m = 16.2 μm, D_a = 2.7 μm) that we predicted would maximize vessel K_{sc} (e.g., Fig. 13).

The pit conductivity (pit K_{sp}) results support the intuitive notion that a greater air-seed pressure results in a lower pit conductivity (Fig. 9A). For capillary-seeding pits, a higher air-seed pressure required denser pit membrane with narrower pores. Although more pores are present per area, each pore is smaller, and the strongly nonlinear pore conductivity vs. pore diameter relationship results in a lower total conductivity of the pit membrane (Fig. 9B, solid symbols). Wall strength (as opposed to pit membrane strength) also influenced the pit conductivity through altering the pit aperture structure. Somewhat nonintuitively, pits in wider conduits were predicted to have lower conductivities than pits in narrow conduits because of the need for thicker walls and hence deeper apertures with greater hydraulic resistance (Fig. 9B). Thus, for the same pit geometry and arrangement, wider conduits will have a lower wall conductivity per wall area than narrower conduits. However, this disadvantage of wide conduits paled in comparison with their advantage in having much higher lumen conductivity. As long as the lumen is long enough to significantly influence the vessel conductivity, wider conduits had a higher vessel K_{sc} than narrow ones across all air-seed pressures (Fig. 12).

The equations we used to predict pit conductivity accurately predicted the conductivity of scale models of pit membranes where the membrane pores could be measured (Fig. 5). The greatest potential error lies in our representation of the membrane porosity. The predicted range of pit membrane conductivities is consistent with estimates from pit membrane digestion experiments (Schulte and Gibson, 1988), but without the air-seed pressure of this experimental material (species of *Dioon*, *Ruscus*, *Trochodendron*, and *Drimys*) a more precise comparison is not possible. Unfortunately, empirical measurements of pit membrane conductivity are very difficult to make,

so until such measurements are available we have little to compare with our calculations at the single pit level. The "single vessel technique" of Zwieniecki et al. (2001b) may be a useful tool in this regard.

An important result of the vessel K_{sc} analysis is the prediction of a "saturating vessel length" above which there is no further increase in the vessel conductivity. This result is similar to the conclusions of Gibson and colleagues indicating that fern tracheid length must increase with diameter for a gain in conductivity to be fully realized (Calkin et al., 1986; Schulte et al., 1987; Schulte and Gibson, 1988). Vessels (or tracheids) longer than the saturating length contribute nothing to hydraulic conductivity and represent a liability in terms of the spread of vascular disease and cavitation (Comstock and Sperry, 2000). The optimal vessel length should be the saturating length. Our results support this intuition, because measured lengths on some of the same species and genera are similar to the saturating lengths predicted from the model (Fig. 11A). The saturating lengths are relatively short, but would be longer if pitting percentage was less than our 50% default (Fig. 10). However, preliminary estimates from our material suggest that about 55% of the wall is pitted. The fact that saturating lengths are generally short may be the reason that observed vessel length distributions are so strongly skewed to short lengths (Zimmermann and Jeje, 1981).

If vessels are at or above their saturating lengths, their conductivity will not be influenced by pit conductivity and should approach the Hagen-Poiseuille value. In fact, measurements of the hydraulic conductivity of progressively shortened angiosperm stems have not shown any increase in conductivity as more pitted walls are removed and water flows through open vessel lumens (Chiu and Ewers, 1993): this result is consistent with the pitted walls having minimal influence on the vessel conductivity. The reason that actual conductivities are usually much less than the Hagen-Poiseuille value (Zimmermann, 1983; Ewers, 1985; Schulte and Gibson, 1988; Chiu and Ewers, 1993) may have more to do with irregular vessel shape and the geometry of the vessel network than with the resistance of pitted walls. The vessel-casting method has revealed that vessels often deviate significantly from being perfect pipes (André, 2002).

Recent work suggests that changes in pit membrane porosity with ionic strength of the xylem sap are responsible for changes in overall xylem conductivity (Zimmermann, 1983; Van Ieperen et al., 2000; Zwieniecki et al., 2001a). However, this can only be possible if vessels are shorter than their saturating lengths. Perhaps the variation between species in the ionic response (an approximate 10% change in many species) are a result of shorter vessel lengths in the more responsive species.

The fact that saturated vessel conductivity is not directly influenced by pit conductivity explains why the trade-off between vessel conductivity and air-seed pressure (Fig. 12) was less steep and more variable than the trade-off between pit conductivity and air-seed pressure (Fig. 9A). The decrease in vessel K_{sc} was solely a result of the greater thickness-to-span ratio required to maintain implosion resistance as air-seed pressure increased. The considerable scatter was because the variation in vessel diameter was independent of air-seed pressure. This result is consistent with numerous observations of a variable relationship between vessel diameter and conductivity per wood area vs. cavitation resistance in a variety of other data sets (Tyree et al., 1994; Pockman and Sperry, 2000; Hacke and Sperry, 2001). If we expressed conductivity solely on a lumen area basis (instead of a wall area basis), there would be no theoretical relationship between vessel conductivity and air-seed pressure, assuming that vessels are long enough to saturate their conductivity.

Although pit conductivity does not directly limit the saturated vessel conductivity, the structure of pits does influence the saturated vessel K_{sc} and the saturating vessel length. The higher the ligament efficiency, the thinner the vessel wall can be for a given implosion pressure and hence the greater the vessel conductivity per wall area invested. The maximum possible vessel K_{sc} at the saturated length for the average vessel (Fig. 13, open symbols at arrow) was achieved by wide pit membranes (D_m = 16.2 μm) and relatively narrow pit apertures (D_a = 2.7 μm) with a high ligament efficiency. With respect to vessel length, the necessarily lower pit conductivity associated with higher air-seed pressure (Fig. 9A) does not by itself reduce the saturated vessel K_{sc}, but it does require a greater vessel length to achieve the saturated K_{sc}. Any structural modification that increases pit conductivity would allow for shorter vessels without costing the plant any xylem conductivity. All else equal, shorter conduits will be beneficial in limiting conductivity losses from damage and cavitation (Comstock and Sperry, 2000) and also in limiting the spread of pathogens.

Clearly, it is an important goal for future work to determine whether in fact vessels are at their saturating lengths as our analysis suggests, and if not, what additional factors or constraints are responsible for this deviation from what should be the optimal vessel length.

There are numerous applications of a quantitative biomechanical approach to xylem structure and function that go beyond what we have attempted here. We confined our analysis to circular bordered pits in opposite pitting fields. However, the approach can be extended to predict the effect of scalariform pitting and the influence of opposite vs. alternate pitting arrangements on conduit wall strength and hydraulic conductivity. From the standpoint of packing a maximum of pit membrane area per conduit wall area, scalariform pitting should be superior, followed by alternate pitting, with opposite pitting being the least efficient (Carlquist, 1988). Balancing these advantages may be the limitations on pit membrane and conduit wall strength.

We also did not model the effect of vestured pitting on pit function (Zweypfennig, 1978). However, considerations of membrane mechanics suggest three advantages of vestured pitting in which the membrane is braced in its flat position by outgrowths of the chamber wall. (1) A braced membrane can be larger in diameter without rupture-seeding, perhaps allowing conduits to approach their maximum K_{sc} more closely. However, the one study species we know that has vestured pits of the appropriate type, *Nerium oleander*, did not have pits any larger than the norm. (2) Vestures prevent membrane stretching and should therefore prevent cavitation fatigue or rupture (Zweypfennig, 1978). (3) No membrane stretching means that the membrane pore size for water conduction is no smaller than the membrane pore size at air-seeding. This translates into a higher membrane hydraulic conductivity per air-seed pressure. These advantages of vestured pitting may outweigh any disadvantage of the vestures in increasing pit hydraulic resistance.

Our primary goal, however, was to compare the analysis of homogenous pit membranes of intervessel pitting to the torus-margo structure of pit membranes in many gymnosperm tra-

cheids. Given that tracheids are necessarily limited in length, their pit membranes should be under increased selection for maximizing pit conductivity. Does the torus-margo membrane provide an advantage in this regard? We attempt to answer this question in the second paper of the series.

LITERATURE CITED

ANDRÉ, J.-P. 2002. Organisation vasculaire des angiospermes: une vision nouvelle. INRA, Paris, France.

ASHBY, M. F., L. J. GIBSON, U. WEGST, AND R. OLIVE. 1995. The mechanical properties of natural materials. I. Material property charts. *Proceedings of the Royal Society of London Series A* 450: 123–140.

BAAS, P. 1986. Ecological patterns of xylem anatomy. *In* T. J. Givnish [ed.], On the economy of plant form and function, 327–351. Cambridge University Press, Cambridge, UK.

BAUCH, J. W., W. LIESE, AND R. SCHULTZE. 1972. The morphological variability of the bordered pit membranes in gymnosperms. *Wood Science and Technology* 6: 165–184.

CALKIN, H. W., A. C. GIBSON, AND P. S. NOBEL. 1986. Biophysical model of xylem conductance in tracheids of the fern *Pteris vittata*. *Journal of Experimental Botany* 37: 1054–1064.

CARLQUIST, S. 1988. Comparative wood anatomy. Springer-Verlag, Berlin, Germany.

CARPITA, N. C., AND D. M. GIBEAUT. 1993. Structural models of primary cell walls in flowering plants: consistency of molecular structure with the physical properties of the walls during growth. *Plant Journal* 3: 1–30.

CHIU, S. T., AND F. W. EWERS. 1993. The effect of segment length on conductance measurements in *Lonicera fragrantissima*. *Journal of Experimental Botany* 44: 175–181.

COCHARD, H., F. FROUX, S. MAYR, AND C. COUTAND. 2004. Xylem wall collapse in water-stressed pine needles. *Plant Physiology* 134: 1–8.

COMSTOCK, J. P., AND J. S. SPERRY. 2000. Tansley review no. 119. Some theoretical considerations of optimal conduit length for water transport in plants. *New Phytologist* 148: 195–218.

CORE, H. A., W. A. COTE, AND A. C. DAY. 1979. Wood structure and identification. Syracuse University Press, Syracuse, New York, USA.

DAGAN, Z., S. WEIBAUM, AND R. PFEFFER. 1982. An infinite-series solution for the creeping motion through an orifice of finite length. *Journal of Fluid Mechanics* 115: 505–523.

DAVIS, S. D., F. W. EWERS, K. A. PORTWOOD, J. S. SPERRY, M. C. CROCKER, AND G. C. ADAMS. 2002. Shoot dieback during prolonged drought in *Ceanothus* chaparral in California: a possible case of hydraulic failure. *American Journal of Botany* 89: 820–828.

DAVIS, S. D., F. W. EWERS, J. WOOD, J. J. REEVES, AND K. J. KOLB. 1999. Differential susceptibility to xylem cavitation among three pairs of *Ceanothus* species in the Transverse Mountain ranges of southern California. *Ecoscience* 6: 180–186.

DAVIS, S. D., K. J. KOLB, AND K. P. BARTON. 1998. Ecophysiological processes and demographic patterns in the structuring of California chaparral. *In* P. W. Rundel, G. Montenegro, and F. Jaksic [eds.], Landscape disturbance and biodiversity in mediterranean-type ecosystems, 297–310. Springer-Verlag, Berlin, Germany.

EWERS, F. W. 1985. Xylem structure and water conduction in conifer trees, dicot trees, and lianas. *International Association of Wood Anatomists Bulletin* 6: 309–317.

EWERS, F. W., AND J. B. FISHER. 1989. Variation in vessel length and diameter in stems of six tropical and subtropical lianas. *American Journal of Botany* 76: 1452–1459.

HACKE, U. G., AND J. S. SPERRY. 2001. Functional and ecological xylem anatomy. *Perspectives in Plant Ecology, Evolution and Systematics* 4: 97–115.

HACKE, U. G., AND J. S. SPERRY. 2003. Limits to xylem refilling under negative pressure in *Laurus nobilis* and *Acer negundo*. *Plant, Cell and Environment* 26: 303–311.

HACKE, U. G., J. S. SPERRY, AND J. PITTERMANN. 2000. Drought experience and cavitation resistance in six desert shrubs of the Great Basin, Utah. *Basic and Applied Ecology* 1: 31–41.

HACKE, U. G., J. S. SPERRY, AND J. PITTERMANN. 2004. Analysis of circular bordered pit function. II. Gymnosperm tracheids with torus-margo pit membranes. *American Journal of Botany* 91: 386–400.

HACKE, U. G., V. STILLER, J. S. SPERRY, J. PITTERMANN, AND K. A. MCCULLOH. 2001b. Cavitation fatigue. Embolism and refilling cycles can weaken the cavitation resistance of xylem. *Plant Physiology* 125: 779–786.

HACKE, U. G., J. S. SPERRY, W. P. POCKMAN, S. D. DAVIS, AND K. A. MCCULLOH. 2001a. Trends in wood density and structure are linked to prevention of xylem implosion by negative pressure. *Oecologia* 126: 457–461.

HARGRAVE, K. R., K. J. KOLB, F. W. EWERS, AND S. D. DAVIS. 1994. Conduit diameter and drought-induced embolism in *Salvia mellifera* Greene (Labiatae). *New Phytologist* 126: 695–705.

HEPWORTH, D. G., AND J. F. V. VINCENT. 1998a. Modelling the mechanical properties of xylem tissue from tobacco plants (*Nicotiana tabacum* "Samsun") by considering the importance of molecular and micromechanisms. *Annals of Botany* 81: 761–770.

HEPWORTH, D. G., AND J. F. V. VINCENT. 1998b. The mechanical properties of xylem tissue from tobacco plants (*Nicotiana tabacum* "Samsun"). *Annals of Botany* 81: 751–759.

JERONIMIDIS, G. 1980. Wood, one of natures challenging composites. *In* J. F V. Vincent and J. D. Curry [eds.], The mechanical properties of biological materials, 169–182. Cambridge University Press, Cambridge, UK.

KOLB, K. J., AND J. S. SPERRY. 1999a. Transport constraints on water use by the Great Basin shrub, *Artemisia tridentata*. *Plant Cell and Environment* 22: 925–935.

KOLB, K. J., AND J. S. SPERRY. 1999b. Differences in drought adaptation between subspecies of sagebrush (*Artemisia tridentata*). *Ecology* 80: 2373–2384.

LANCASHIRE, J. R., AND A. R. ENNOS. 2002. Modelling the hydrodynamic resistance of bordered pits. *Journal of Experimental Botany* 53: 1485–1493.

LO GULLO, M. A., AND S. SALLEO. 1993. Different vulnerabilities of *Quercus ilex* L. to freeze- and summer drought-induced xylem embolism: an ecological interpretation. *Plant Cell and Environment* 16: 511–519.

MARK, R. E. 1967. Cell wall mechanics of tracheids. Yale University Press, New Haven, Connecticut, USA.

MARTINEZ-VILALTA, J., E. PRAT, I. OLIVERAS, AND J. PINOL. 2002. Xylem hydraulic properties of roots and stems of nine Mediterranean woody species. *Oecologia* 133: 19–29.

MENCUCCINI, M., AND J. COMSTOCK. 1997. Vulnerability to cavitation in populations of two desert species, *Hymenoclea salsola* and *Ambrosia dumosa*, from different climatic regions. *Journal of Experimental Botany* 48: 1323–1334.

O'DONNELL, W. J., AND B. F. LANGER. 1962. Design of perforated plates. *ASME Journal of Engineering for Industry, Transactions of the ASME. Series B* 84: 307–320.

PANSHIN, A. J., AND C. DE ZEEUW. 1970. Textbook of wood technology. McGraw-Hill, New York, New York, USA.

PETTY, J. A. 1972. The aspiration of bordered pits in conifer wood. *Proceedings of the Royal Society of London, Series B* 181: 395–406.

PICKARD, W. F. 1981. The ascent of sap in plants. *Progress in Biophysics and Molecular Biology* 37: 181–229.

PIQUEMAL, J., C. LAPIERRE, K. MYTON, A. O'CONNEL, W. SCHUCH, J. GRIMA-PETTENATI, AND A. M. BOUDET. 1998. Down-regulation of cinnamoyl-CoA reductase induces significant changes of lignin profiles in transgenic tobacco plants. *Plant Journal* 13: 71–83.

POCKMAN, W. T., AND J. S. SPERRY. 2000. Vulnerability to xylem cavitation and the distribution of Sonoran Desert vegetation. *American Journal of Botany* 87: 1287–1299.

POCKMAN, W. T., J. S. SPERRY, AND J. W. O'LEARY. 1995. Sustained and significant negative water pressure in xylem. *Nature* 378: 715–716.

SALLEO, S., AND M. A. LO GULLO. 1989. Different aspects of cavitation resistance in *Ceratonia siliqua*, a drought-avoiding Mediterranean tree. *Annals of Botany* 64: 325–336.

SCHULTE, P. J., AND A. C. GIBSON. 1988. Hydraulic conductance and tracheid anatomy in six species of extant seed plants. *Canadian Journal of Botany* 66: 1073–1079.

SCHULTE, P. J., A. C. GIBSON, AND P. S. NOBEL. 1987. Xylem anatomy and hydraulic conductance of *Psilotum nudum*. *American Journal of Botany* 74: 1438–1445.

SIAU, J. F. 1971. Flow in wood. Syracuse University Press, Syracuse, New York, USA.

SIAU, J. F., R. W. DAVIDSON, J. A. MEYER, AND C. SKAAR. 1984. Transport processes in wood. Springer, Berlin, Germany.

SMART, C. C., AND N. AMRHEIN. 1985. The influence of lignification on the development of vascular tissue in *Vigna radiata* L. *Protoplasma* 124: 87–95.

SPERRY, J. S., J. R. DONNELLY, AND M. T. TYREE. 1988. A method for measuring hydraulic conductivity and embolism in xylem. *Plant Cell and Environment* 11: 35–40.

SPERRY, J. S., AND U. G. HACKE. 2002. Desert shrub water relations with respect to soil characteristics and plant functional type. *Functional Ecology* 16: 367–378.

SPERRY, J. S., K. L. NICHOLS, J. E. M. SULLIVAN, AND S. E. EASTLACK. 1994. Xylem embolism in ring-porous, diffuse-porous, and coniferous trees of northern Utah and interior Alaska. *Ecology* 75: 1736–1752.

SPERRY, J. S., AND N. Z. SALIENDRA. 1994. Intra-and inter-plant variation in xylem cavitation in *Betula occidentalis*. *Plant, Cell and Environment* 17: 1233–1241.

SPERRY, J. S., AND J. E. M. SULLIVAN. 1992. Xylem embolism in response to freeze-thaw cycles and water stress in ring-porous, diffuse-porous, and conifer species. *Plant Physiology* 100: 605–613.

SPERRY, J. S., AND M. T. TYREE. 1988. Mechanism of water stress-induced xylem embolism. *Plant Physiology* 88: 581–587.

STILLER, V., H. R. LAFITTE, AND J. S. SPERRY. 2003. Hydraulic properties of rice (*Oryza sativa* L.) and the response of gas exchange to water stress. *Plant Physiology* 132: 1698–1706.

STILLER, V., AND J. S. SPERRY. 2002. Cavitation fatigue and its reversal in intact sunflower plants. *Journal of Experimental Botany* 53: 1155–1161.

THOMAS, R. J. 1972. Bordered pit aspiration in angiosperms. *Wood and Fiber* 3: 236–237.

TIO, K. K., AND S. S. SADHAL. 1994. Boundary conditions for stokes flows near a porous membrane. *Applied Scientific Research* 52: 1–20.

TURNER, S. R., AND C. R. SOMERVILLE. 1997. Collapsed xylem phenotype of Arabidopsis identifies mutants deficient in cellulose deposition in the secondary cell wall. *Plant Cell* 9: 689–701.

TYREE, M., S. DAVIS, AND H. COCHARD. 1994. Biophysical perspectives of xylem evolution—is there a tradeoff of hydraulic efficiency for vulnerability to dysfunction? *International Association of Wood Anatomists Journal* 15: 335–360.

VAN IEPEREN, W., U. VAN MEETEREN, AND H. VAN GELDER. 2000. Fluid ionic composition influences hydraulic conductance of xylem conduits. *Journal of Experimental Botany* 51: 769–776.

VINCENT, J. F. V. 1999. From cellulose to cell. *Journal of Experimental Biology* 202: 3263–3268.

VOGEL, S. 1994. Life in moving fluids: the physical biology of flow. Princeton University Press, Princeton, New Jersey, USA.

YOUNG, W. C. 1989. Roark's formulas for stress and strain. McGraw Hill, New York, New York, USA.

ZIMMERMANN, M. H. 1983. Xylem structure and the ascent of sap. Springer-Verlag, Berlin, Germany.

ZIMMERMANN, M. H., AND A. A. JEJE. 1981. Vessel length distribution of some American woody plants. *Canadian Journal of Botany* 59: 1882–1892.

ZIMMERMANN, M. H., AND D. POTTER. 1982. Vessel length distribution in branches, stem, and roots of *Acer rubrum*. *International Association of Wood Anatomists Bulletin* 3: 103–109.

ZWEYPFENNIG, R. C. V. J. 1978. A hypothesis on the function of vestured pits. *International Association of Wood Anatomists Bulletin* 1: 13–15.

ZWIENIECKI, M. A., P. J. MELCHER, AND N. M. HOLBROOK. 2001a. Hydrogel control of xylem hydraulic resistance in plants. *Science* 291: 1059–1062.

ZWIENIECKI, M. A., P. J. MELCHER, AND N. M. HOLBROOK. 2001b. Hydraulic properties of individual xylem vessels of *Fraxinus americana*. *Journal of Experimental Botany* 52: 257–264.